AGU PUBLICATIONS

JGR

Journal of Geophysical Research: Solid Earth

RESEARCH ARTICLE
10.1002/2017JB014014

The Effect of Water Column Resonance on the Spectra of Secondary Microseism *P* Waves

Matthias Meschede[1], **Éléonore Stutzmann**[1], **Véronique Farra**[1], **Martin Schimmel**[2], **and Fabrice Ardhuin**[3]

[1]Institut de Physique du Globe de Paris, Paris, France, [2]Institut of Earth Sciences Jaume Almera-CSIC, Barcelona, Spain, [3]University of Brest, CNRS, IRD, Ifremer, Laboratoire d'Océanographie Physique et Spatiale, IUEM, Brest, France

Key Points:
- Double peak in secondary microseism spectra is a consequence of water column resonance
- Observed and modeled spectra of secondary microseisms can be quantitatively compared
- Water column resonance has to be taken into account to model secondary microseism body waves

Supporting Information:
- Supporting Information S1

Correspondence to:
M. Meschede,
meschede@ipgp.fr

Citation:
Meschede, M., Stutzmann, É., Farra, V., Schimmel, M., & Ardhuin, F. (2017). The effect of water column resonance on the spectra of secondary microseism *P* waves. *Journal of Geophysical Research: Solid Earth*, *122*, 8121–8142. https://doi.org/10.1002/2017JB014014

Received 23 JAN 2017
Accepted 13 SEP 2017
Accepted article online 19 SEP 2017
Published online 26 OCT 2017

Abstract We compile and analyze a data set of secondary microseismic *P* wave spectra that were observed by North American seismic arrays. Two distinct frequency bands, 0.13–0.15 Hz and 0.19–0.21 Hz, with enhanced *P* wave energy characterize the data set. Cluster analysis allows to classify the spectra and to associate typical spectral shapes with geographical regions: Low-frequency-dominated spectra (0.13–0.15 Hz) are mostly detected in shallower regions of the North Atlantic and the South Pacific, as well as along the Central and South American Pacific coast. High-frequency-dominated spectra (0.19–0.21 Hz) are mostly detected in deeper regions of the northwestern Pacific and the South Pacific. For a selected subset of high-quality sources, we compute synthetic spectra from an ocean wave hindcast. These synthetic spectra are able to reproduce amplitude and shape of the observed spectra, but only if *P* wave resonance in the water column at the source site is included in the model. Our data sets therefore indicate that the spectral peaks at 0.13–0.15 Hz and 0.19–0.21 Hz correspond to the first and second harmonics of *P* wave resonance in the water column that occur in shallower ocean depths (<3,000 m) and in the deep ocean (~5,000 m), respectively. This article demonstrates the important effect of water column resonance on the amplitude and frequency of *P* waves that are generated by secondary microseisms and that the amplitude of high-quality sources can be predicted from ocean wave hindcasts within a factor of 0.4–6.

1. Introduction

Since the first discoveries of secondary microseismic signals (e.g., Bertelli, 1872), numerous studies have contributed to the understanding of their origins and composition (see, e.g., historical review by Ebeling, 2012).

Most seismic energy in the secondary microseism frequency band from 0.1 to 0.3 Hz is associated with the interaction of opposing ocean waves (Hasselmann, 1963; Longuet-Higgins, 1950). Rayleigh waves and local, regional, and teleseismic *P* waves have been identified at these frequencies that likely originate from this mechanism (for Rayleigh waves see, e.g., Friedrich et al., 1998; Schimmel et al., 2011; Schulte-Pelkum et al., 2004; Stehly et al., 2006; Stutzman et al., 2009, and for body waves, e.g., Gerstoft et al., 2006, 2008; Haubrich & McCamy, 1969; Koper et al., 2009, 2010; Landès et al., 2010; Obrebski et al., 2013; Toksöz & Lacoss, 1968; Zhang, Gerstoft, & Bromirski, 2010). Love waves (Hadziioannou et al., 2012; Nishida et al., 2008; Tanimoto et al., 2015) and horizontally polarized *S* waves (Liu et al., 2016; Nishida & Takagi, 2016) have also been reported, but their generation mechanism remains unclear.

Analysis of surface or body waves has robustly identified different origins of ocean wave interactions, such as storms, coastal reflections, or opposing swell systems (e.g., Ardhuin et al., 2011; Gerstoft et al., 2006, 2008; Obrebski et al., 2013; Stutzmann et al., 2012). In addition, amplification of surface or body waves due to resonance at specific water depths has been associated with the preferential observation of microseismic sources at certain locations (e.g., Ardhuin et al., 2011; Euler et al., 2014; Gualtieri et al., 2014; Kedar et al., 2008; Stutzmann et al., 2012).

On the basis of the theoretical studies of seismic wave excitation due to ocean wave interactions (Hasselmann, 1963; Longuet-Higgins, 1950), quantitative modeling of surface wave energy spectra from an ocean wave hindcast has been shown to predict recorded noise spectra in the secondary microseism band (Ardhuin et al., 2011; Kedar et al., 2008; Stutzmann et al., 2012). Unfortunately, the source region is not readily accessible

because surface waves provide access to the azimuth but not to the distance between a seismic station (or array) and the source.

Forty years ago, Vinnik (1973) showed the first modeling of *P* waves generated by secondary microseism sources, but he neglected resonance effects in the ocean water column. Recently, Ardhuin and Herbers (2013), Farra et al. (2016), and Nishida and Takagi (2016) proposed more accurate modeling of the energy spectra of secondary microseism *P* waves. These advances allow us to perform an assessment of recorded *P* wave spectra, with the major advantage with respect to surface waves that their origin can be localized using standard array processing techniques. This allows for a direct comparison with position, frequency, and energy of sources that are predicted from an ocean wave model.

In this study, we systematically extract secondary microseism *P* wave spectra from 5 years of seismic data recorded by North American arrays using beamforming techniques. We compute corresponding synthetic *P* wave spectra from ocean wave hindcasts (Ardhuin et al., 2011) using the formalism developed by Farra et al. (2016). We statistically assess the accuracy of the modeled spectra by comparing them with observations in terms of spectral shape and amplitude. We show that secondary microseism *P* wave energy is preferentially concentrated around two distinct frequency peaks at 0.14 Hz and 0.20 Hz and that these spectral peaks are associated with *P* waves from particular geographical regions. We explain these particular spectral shapes as a consequence of water column resonance at different ocean depths. Our analysis shows that water column resonance is essential to understand the origin, amplitude, and spectral shape of observed *P* waves from secondary microseisms.

2. Data and Methodology

2.1. Data

Our data set consists of continuous vertical-component ground-motion data sampled at 1 Hz, recorded over a combined timespan of 5 years by the five different North American arrays shown in Figure 1a. We obtain data from the Incorporated Research Institutions for Seismology (IRIS) data management center for the year 2015 from the AK, AT, and TA networks (hereinafter "Alaska"), for the year 2015 from network CI ("California"), for the year 2008 from network XC ("Lavaplains"), for the year 2011 from network YX ("Nevada"), and for the year 2006 from networks XF and ZA ("Mexico") (see acknowledgments for detailed references). Note that not all days are available for all stations of these arrays during these years.

We deconvolve the instrument response function from the raw recordings and end up with continuous ground displacement time series with flat frequency response in the secondary microseismic band (0.05–0.30 Hz). Considering that we only use *P* waves in the distance range from about 30 to 90° from the arrays, our data set covers the area shown in Figure 1b, where the blue color intensity indicates the number of arrays that can see a specific position. *P* waves from distances shorter than 30° or farther than 90° are not considered in this study because their amplitudes are difficult to model within our theoretical framework. The spatial coverage that we obtain with the arrays used in this study allows to make independent observations of the same source regions ensuring robust observations.

2.2. Beamforming

The central quantity of this article is the day averaged power spectral density $B(f, \mathbf{s})$ (*beam PSD*) at frequency f and horizontal slowness $\mathbf{s}$ of the vertical component ground displacement recorded by a seismic array. $B(f, \mathbf{s})$ can be seen as the plane wave energy that arrives at the array with a certain frequency and horizontal slowness from a specific direction. Such plane waves can be potentially associated with the wavefront of a distant point source. In case of a body wave with secondary microseismic origin this point source is localized at the intersection of the wave's raypath and the surface of the Earth. We compute the beam PSD using a standard beamforming approach that we summarize in the following paragraphs (for an extensive introduction see, e.g., Rost & Thomas, 2002).

Initially, a subwindow beam PSD $B_w(f, \mathbf{s})$ is computed in time windows of length 128 s from the traces that are recorded by the stations in the array. In each window, traces are discarded whose standard deviation is larger than 2 times the median standard deviation of all traces of the array. This selection process removes stations with potentially corrupted data, such that we end up with N traces $S_j(t)$ that have consistent amplitudes, where j indicates the station index within the array.

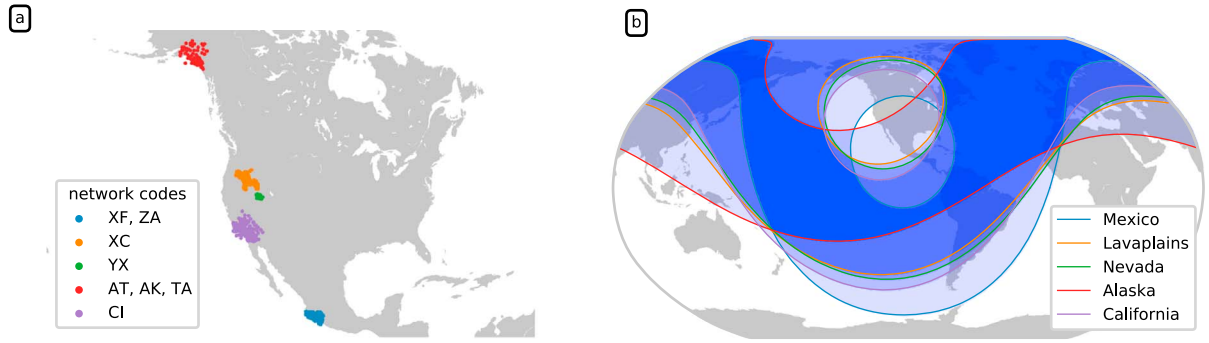

Figure 1. (a) Seismic arrays in North America that have been used to gather continuous data for a combined timespan of 5 years. We use the following terms for these seismic networks: Alaska refers to AK, AT, TA (2015), California to CI (2015), Mexico to XF, ZA (2006), LavaPlains to XC (2008), and Nevada to YX (2009). (b) Array coverage. We study *P* waves in the distance range 30°–90° around each array. The intensity of blue color indicates how many arrays see a region.

$B_w(f, \mathbf{s})$ is then computed on a square Cartesian slowness grid in the range −0.1–0.1 s/km and in the frequency band from 0.08 to 0.30 Hz that comprises the slowness range of *P* waves and the frequency band of the secondary microseismic peak.

To compute $B_w(f, \mathbf{s})$, the Fourier spectra $S_j(f)$ are phase aligned by multiplication with $e^{-i2\pi f \mathbf{s}\cdot(\mathbf{x}_j-\mathbf{x}_c)}$ at each grid point $\mathbf{s}$. Here $\mathbf{x}_j$ and $\mathbf{x}_c$ are the positions of station j and the array center, respectively. The mean over these phase-aligned Fourier spectra approximates the Fourier spectrum of the plane waves that arrive at the array center with slowness $\mathbf{s}$. $B_w(f, \mathbf{s})$ is their power spectral density with unit (m^2/Hz):

$$B_w(f, \mathbf{s}) = \frac{1}{N^2}\left|\sum_{j=1}^{N} S_j(f) e^{-i2\pi f \mathbf{s}\cdot(\mathbf{x}_j-\mathbf{x}_c)}\right|^2. \quad (1)$$

$B_w(f, \mathbf{s})$, as calculated in equation (1), depends not only on the phase of the arriving waves but also on their amplitude. Therefore, strong incoherent energy can potentially lead to larger values than weak coherently arriving plane waves. We introduce here an extra weight factor $w(f, \mathbf{s})$, which measures the coherency of the incoming wavefield independently of its amplitude. We use the phase stack to define this coherency factor (Schimmel & Gallart, 2007; Schimmel & Paulssen, 1997):

$$w(f, \mathbf{s}) = \frac{1}{N^2}\left|\sum_{j=1}^{N} \frac{S_j(f)}{|S_j(f)|} e^{-i2\pi f \mathbf{s}\cdot(\mathbf{x}_j-\mathbf{x}_c)}\right|^2. \quad (2)$$

The weight factor $w(f, \mathbf{s})$ is one for perfectly coherent plane waves and drops to a small value otherwise. The final *phase-weighted* beam PSD reduces incoherently arriving energy and is constructed as

$$B_{pw}(f, \mathbf{s}) = w(f, \mathbf{s}) B_w(f, \mathbf{s}). \quad (3)$$

Importantly, the phase-weighted beam PSD of a coherently arriving plane wave is unchanged compared to the unweighted beam PSD. Strong signals that are not coherent over the whole array are suppressed by this procedure. Such signals can have high amplitude and contaminate the beam PSD. Because the microseismic body wave signals are not perfectly coherent plane waves, the observed beam PSD might be slightly biased toward lower amplitudes. In our experience the amplitude bias that is introduced with the phase weight is only on the order of few percent. At the same time, it increases the slowness resolution of the beam and removes incoherent sources.

The beam PSD can be seen as a collection of spectra (PSDs), that is, one PSD at each slowness. Most of the time, the PSDs that are examined in this article have a single spectral peak. We will see that this is not always but most of the time the case for secondary microseisms (see also Neale et al., 2017). We can therefore use two simple parameters to describe the PSD: the PSD's *amplitude* refers to the maximum of the PSD and the PSD *frequency* or *dominant frequency* refers to the frequency of the PSD maximum. This representation allows to use a 2-D image as a compact visualization of the beam PSD, or more specifically of the beam PSD spectral peak: color lightness is used to show the beam PSD amplitude, and color hue for the beam PSD frequency (for more information on the 2-D color maps see Meschede & Stutzmann, 2016).

The data set is reduced further by averaging the 128 s subwindow beam PSDs B_{pw} over full days, that is, from 00 h to 24 h. Before averaging, however, we remove subwindows that are potential outliers, that is, subwindows that contain a lot more energy than the other subwindows of the day and that is unlikely to originate from secondary microseisms. To this end, we compute a single intensity value for each subwindow from B_{pw}, defined as the sum of the beam PSD amplitudes of all slownesses (from −0.1 s/km to 0.1 s/km). A subwindow is considered valid if the intensity value is smaller than 2 times and greater than 1/1,000 times the median intensity value of the day. Only valid subwindows are used for the daily average.

This selection procedure effectively removes (smaller to intermediate) earthquakes and other short-duration outliers that are, for example, caused by local noise at the array. If most subwindows during a day are noisy due to larger earthquakes or other regional noise, the median intensity value rises and the selection criterion does not discard this day. We therefore end up with some noisy beam PSDs in our data set. The day average of the observed beam PSD is denoted $B(f, \mathbf{s})$ and from now on just called *observed beam PSD*.

Typical beam PSD amplitudes are high only around the few slowness values where plane waves add coherently. The beam PSD amplitude at slowness values away from these peaks corresponds to random fluctuations because here the plane waves add incoherently in addition to other random noise. The median of the beam PSD amplitudes (from −0.1 to 0.1 s/km) is a good measure of the amplitude level of these random fluctuations. The median therefore defines a reasonable threshold below which signals cannot be detected (from now on called noise level of the beam). To enhance the visual perception of the signals of interest, white color indicates in some figures amplitudes below the noise level of the beam rather than zero (indicated by *NL* in plot color bar labels).

To stabilize the beam PSD amplitudes, we smooth it over a narrow frequency band of about 0.04 Hz (Hanning window with width 0.08 Hz) before computing the beam PSD maxima at each slowness. Very narrowband sources with bandwidths of less than 0.04 Hz are attenuated by this procedure. To compute the dominant frequency of the PSD, we use the original unsmoothed spectra.

2.3. Synthetic Beams

We use the ray theoretical approach proposed by Farra et al. (2016) to compute the *synthetic beam PSD* $B_{syn}(f, \mathbf{s})$ from global microseism pressure PSD models that are derived from the ocean wave hindcast WAVEWATCH III (Ardhuin et al., 2011; Rascle & Ardhuin, 2013; Tolman, 2009) and openly distributed. Modeling consists in three essential steps, described in detail in Farra et al. (2016) that are summarized in Figure 2 and described hereafter.

First, we compute $F_p(f, \mathbf{x})$, the power spectral density of the pressure fluctuations (*pressure PSD*) that are generated by wave-wave interactions, that is, the power per frequency f and horizontal wave vector $\mathbf{k}$ with unit ($Pa^2/(m^{-2}$ Hz)) at position $\mathbf{x}$. Pressure fluctuations at frequency f and wave vector $\mathbf{k}$ are generated by interacting ocean waves with frequency f_1, f_2 and wave vectors $\mathbf{k}_1$, $\mathbf{k}_2$, where $f = f_1 + f_2$ and $\mathbf{k} = \mathbf{k}_1 + \mathbf{k}_2$. Only nearly opposing ocean waves with $\mathbf{k}_1 \approx -\mathbf{k}_2$ and $f_1 \approx f_2 \approx f/2$ generate the pressure fluctuations that are necessary to excite seismic waves. Based on statistical hypotheses about the ocean wave height spectrum, F_p is independent of $\mathbf{k}$ in the range of wave vectors that correspond to seismic *P* waves, and the pressure fluctuations are spatially uncorrelated on scales that are larger than the wavelength of seismic *P* waves in water (Hasselmann, 1963).

With these assumptions, F_p is computed from the ocean wave height energy spectrum $E(\mathbf{x}, f/2)$ and its directional distribution function $M(\mathbf{x}, f/2, \phi)$ with azimuth ϕ. E and M are provided by the ocean wave hindcast (for details see Tolman, 2009). Computing F_p from E and M consists essentially in an integration of the ocean wave height energy spectrum over opposite azimuth ϕ (Ardhuin et al., 2011; Hasselmann, 1963):

$$F_p(\mathbf{x}, f) = [2\pi]^2 [\rho_w g]^2 f E^2(f/2) \times \int_0^{\pi} M(f/2, \phi) M(f/2, \phi + \pi)\, \mathrm{d}\phi. \tag{4}$$

Here ρ_w is the water density and g the gravitational acceleration at the surface of the Earth. The resulting pressure PSD field has twice the frequency than the interacting waves. Ocean waves without opposing counterpart do not generate a pressure perturbation that can be observed seismically.

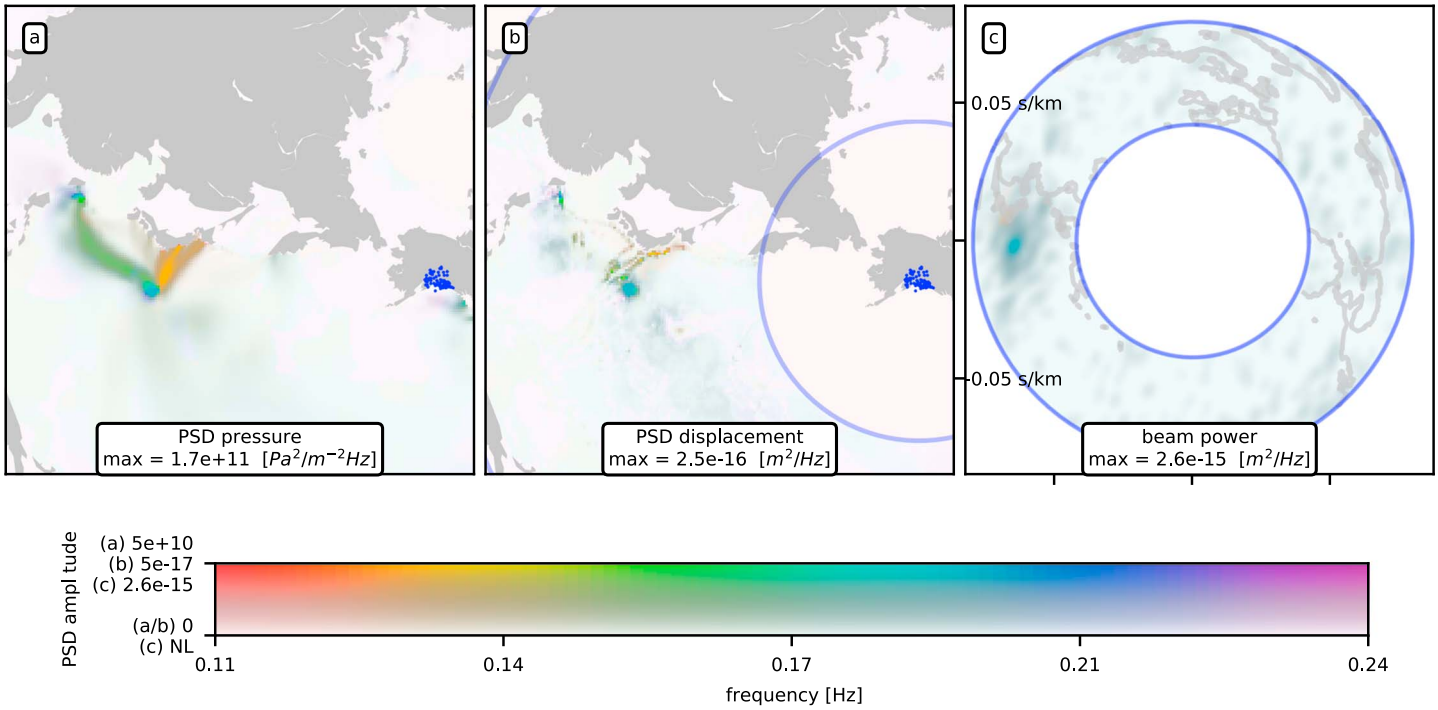

Figure 2. Example of synthetic beam construction for the Alaska array on 23 August 2015. (a) Pressure PSD (saturated colors) that is obtained from model *R*. (b) Displacement PSD (saturated colors) at the array center due to the pressure PSD shown in Figure 2a backprojected on map. The minimum of the color map (white color) is set to zero in Figures 2a and 2b. The color map saturates the PSD amplitudes at 5×10^{10} $Pa^2/m^{-2}Hz$ (Figure 2a) and at 5×10^{-17} m^2/Hz (Figure 2b). The displacement PSD amplitudes that are greater than 1×10^{-17} m^2/Hz are taken into account to compute the synthetic beam PSD shown in Figure 2c. In Figure 2c the color map minimum (white color) is set to the noise level (NL) of the beam that is about 1/7 of the strongest beam PSD amplitude. In Figures2a–2c blue circles delimit the *P* wave distance range that we consider (30°–90°).

Figure 2a shows the pressure PSD field for 23 August 2015, shown from the perspective of the Alaska array. As explained in the previous section, the pressure PSD is characterized at each position by the PSD maximum (*pressure PSD amplitude*), shown by the color lightness, and the frequency of the PSD maximum (*pressure PSD frequency*), shown by the color hue.

In Figure 2a, two strong pressure sources with a dominant frequency of about 0.20 Hz (turquoise color) can be seen that are generated by the two typhoons Goni off the coast of Taiwan and Atsani off the coast of Japan. Furthermore, there are strong wave interactions in between both typhoons that generate pressure sources with a dominant frequency of approximately 0.16 Hz (green) and significant sources due to ocean wave coastal reflections around 0.13 Hz (orange/yellow).

Figure 2b shows the vertical ground displacement PSD amplitude, backprojected on a map, that a seismic station located at the array center would record due to the pressure PSD shown in Figure 2a. Propagation effects, such as geometrical spreading and attenuation, are computed here using a ray tracing formalism (Farra et al., 2016) in the model IASP91 (Kennett & Engdahl, 1991) combined with an attenuation model of Montagner and Kennett (1996).

At a particular position or slowness, these propagation effects transform the pressure PSD in a smooth and systematic way. On the other hand, water column resonance at the source site can sharply amplify the PSD of *P* waves that are radiated from a pressure fluctuation at the ocean surface in the vicinity of a particular frequency. Resonance occurs if a *P* wave that is reflected from the ocean bottom and back from the free surface adds constructively to the wavefield. Multiple reflections within the water column can then lead to strong amplification.

An estimate of the resonance frequencies can be obtained in the case of vertically traveling *P* waves. In this case, the reflected waves accumulate phase corresponding to the two-way travel time in the ocean with depth

h and an additional phase shift of π due to the free surface reflection. Constructive interference takes place when the total accumulated phase corresponds to $2\pi n$, where n is a positive integer number. With wavelength λ in the water, this can be written as

$$2\pi(2h/\lambda) + \pi = 2\pi n \tag{5}$$

or alternatively as

$$h/\lambda = (2n - 1)/4. \tag{6}$$

Resonance therefore occurs approximately when the ocean depth corresponds to 1/4, 3/4, 5/4, … , of the P wave wavelength. Assuming a P wave water velocity of $\alpha_{\text{water}} = 1,500$ m/s, ocean depths of 6,000 m generate resonances around frequencies 0.06 Hz, 0.19 Hz, 0.31 Hz, … , ocean depths of 4,000 m generate resonances at 0.09 Hz, 0.28 Hz, … , and ocean depths of 2,500 m at 0.15 Hz, 0.45 Hz, …. Only few of these resonance peaks are in the frequency band of interest where the pressure PSD F_p has significant energy (0.10–0.24 Hz). In particular, we deal with the resonance peaks for $n = 1$ (0.15 Hz) at ocean depths of 2,500 m depth and $n = 2$ (0.19 Hz) at ocean depths of 6,000 m. Intermediate frequencies (0.16–0.18 Hz) are amplified by shallower depths than 2,500 m through the $n = 1$ resonance or larger depths than 6,000 m through the $n = 2$ resonance.

Nonvertical P waves can be taken into account replacing the ocean wave height h by an effective height $h_\theta = h/\cos(\theta)$, where θ is the angle between raypath direction in the water and the vertical axis. Typical values of θ for P waves are 3.5°–6.8° in the 30°–90° distance range, which does not change the resonance frequency much compared to the vertical case (see Gualtieri et al., 2014).

To compute the magnitude of the amplification factor as a function of frequency, the sum of all P waves, which are multiply reflected and then transmitted in the solid Earth, can be evaluated as a geometric series, as described in detail in Gualtieri et al. (2014). The magnitude of the amplification factor depends on the P wave reflection and transmission coefficients that we compute using a simple 1-D model with a water layer over a solid half-space. The 1-D model is defined with the following structural parameters:

$$\rho_{\text{solid}} = 2,500 \text{ kg/m}^3,\ \rho_{\text{water}} = 1,000 \text{ kg/m}^3,\ \beta_{\text{solid}} = 3,200 \text{ m/s},\ \alpha_{\text{solid}} = 5,540 \text{ m/s, and } \alpha_{\text{water}} = 1,500 \text{ m/s}.$$

Figure 3a shows the P wave amplification factor for slowness 0.05 s/km, computed for three different water depths in the spectral range of interest (0.10–0.24 Hz). At depths characteristic of mid-ocean ridges (2,980 m in Figure 3a) it has a broad resonance peak around 0.13 Hz corresponding to $n = 1$ in equation (6). At intermediate depths (4,116 m in Figure 3a) the amplification factor has no resonance peak in the frequency range of interest because the $n = 1$ resonance frequency is too low and the $n = 2$ resonance frequency too high. The amplification factor at deep ocean depths (5,804 m in Figure 3a) has a sharp high-frequency resonance peak around 0.19 Hz, corresponding to $n = 2$ in equation (6). The 0.13 Hz resonance peak is broader than the 0.19 Hz peak because the accumulated phase of the reflected P wave before interference is proportional to the product of frequency f and ocean depth h. Therefore, the width of the resonance peak is inversely proportional to the ocean depth.

In Figure 2b, the low-frequency coastal reflection sources, as well as typhoon Goni close to Taiwan and the sources that connect both typhoons are strongly damped compared to Figure 2a. In these source regions, the frequencies with significant source pressure PSD do not correspond to the resonance frequencies of the water column.

Site amplification can modulate the recorded P wave amplitude from a factor of 0.4 to 3.7 and the beam PSD by the square of this factor from 0.16 to 14. Nevertheless, the variations of source pressure due to the interacting ocean waves can attain similar orders of magnitude, and it is the combination of the pressure PSD and the amplification factor that controls the amplitude and spectral shape of the radiated P wave.

Figure 3b shows a map of the resonance frequencies within the frequency band of interest (0.10–0.24 Hz). Different symbols indicate the locations with the amplification factor shown in Figure 3a. There are two major resonance frequencies in the oceans: high-frequency resonance (0.18–0.22 Hz) in the deep oceans corresponding to $n = 2$ (bluish color) and low-frequency resonance corresponding to $n = 1$ (0.10–0.15 Hz) in shallower parts over ridges (red and yellow color). Intermediate-frequency resonance (green color) is rare; very shallow coastal regions and intermediate depth ranges do not amplify P wave energy with frequencies

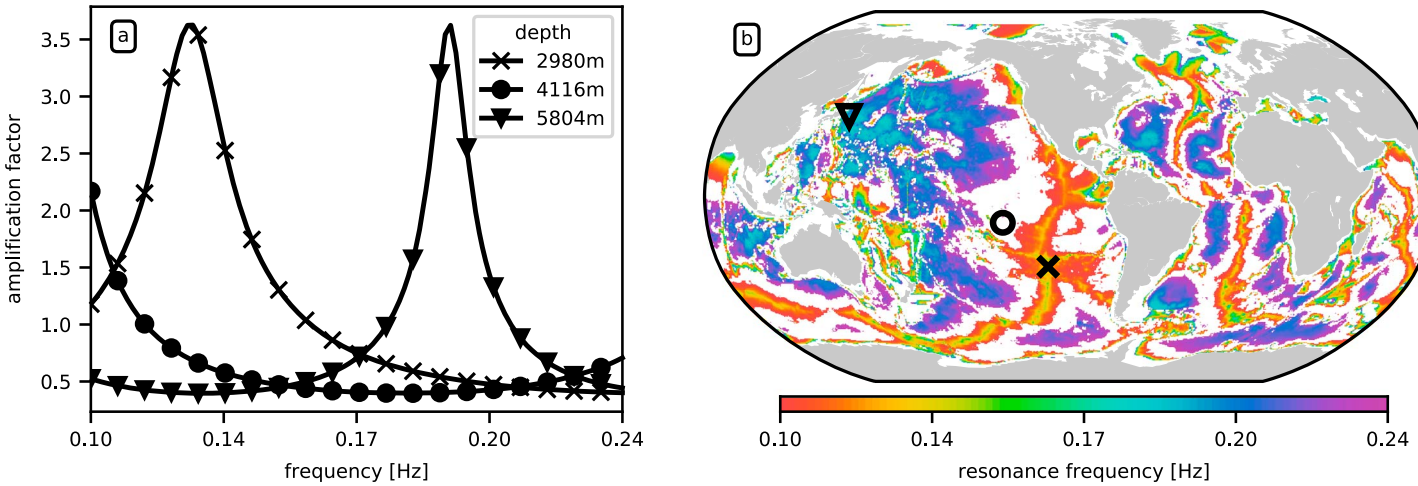

Figure 3. (a) *P* wave amplitude amplification due to water column resonance as a function of frequency for three different ocean depths, computed for slowness 0.05 s/km in a simple two-layer model. (b) Map of the corresponding resonance frequencies in the frequency band of interest (0.10–0.24 Hz) and at slowness 0.05 s/km. The position of the three examples from Figure 3a are indicated with the corresponding symbols in the map.

in the band of interest. If ocean wave pressure sources were distributed evenly over the ocean and all frequencies, we would expect secondary microseismic *P* wave energy to be predominantly concentrated in the high-frequency and some in the low-frequency peaks.

Finally, the computed *P* wave displacement PSD from each grid point is convolved in slowness space with the array response. The sum of all sources whose displacement PSD is greater than a specified threshold (10^{-17} m^2/Hz) yields the *synthetic beam PSD* B_{syn} shown in Figure 2c. The synthetic beam PSD has only a single peak with a single color in contrast to Figures 2a and 2b. At most slownesses the beam PSD amplitude corresponds to random fluctuations with a beam PSD frequency that is the same as at the isolated peak. These random fluctuations can be seen as the noise level of the beam that is at about 1/7 of the strongest beam PSD amplitude in this particular case. The noise level is controlled by the beam PSD amplitude of the strongest source, the overall number of sources, the geometry of the array, and our beamforming technique. In this specific case the noise that corresponds to the strongest source dominates all other sources that are weaker. Multiple sources can only be analyzed if they have comparable amplitude. We therefore focus in this article only on the strongest source of a particular day.

The spatial beam PSD resolution, controlled by the aperture of the arrays that have been used for this study, is much lower than the spatial resolution of the ocean wave model. Therefore, the synthetic beam PSD corresponds to a smoothed version of the vertical displacement PSD that has been computed in step two.

In this article we use and compare three different models for B_{syn} that vary (a) the effect of ocean wave coastal reflections; coastal reflections are either included in the ocean wave hindcast as coastal reflection coefficients of 10% along continents, 20% at island, and 40% at icebergs, or completely excluded; and (b) the effect of water column resonance. The amplification factor is either computed as described above or neglected by setting it everywhere and at all frequencies to one.

Model R, the most comprehensive model, includes coastal reflections and water column resonance. *Model NR* includes water column resonance but no coastal reflections. *Model NA* includes coastal reflections but no water column resonance. Each of the models NR and NA switches off one of the two major factors of the modeling procedure whose influence we would like to examine.

3. Observations

3.1. Individual Days

Figure 4 illustrates the observed beam PSD *B* and the synthetic beam PSD B_{syn} of model *R* for day 12 March 2015. The first row shows $B(f, \mathbf{s})$ (a) and model R $B_{syn}(f, \mathbf{s})$ (b) in slowness domain. The beam PSD amplitude (narrowband smoothed) is displayed with color lightness and the beam PSD frequency with color hue.

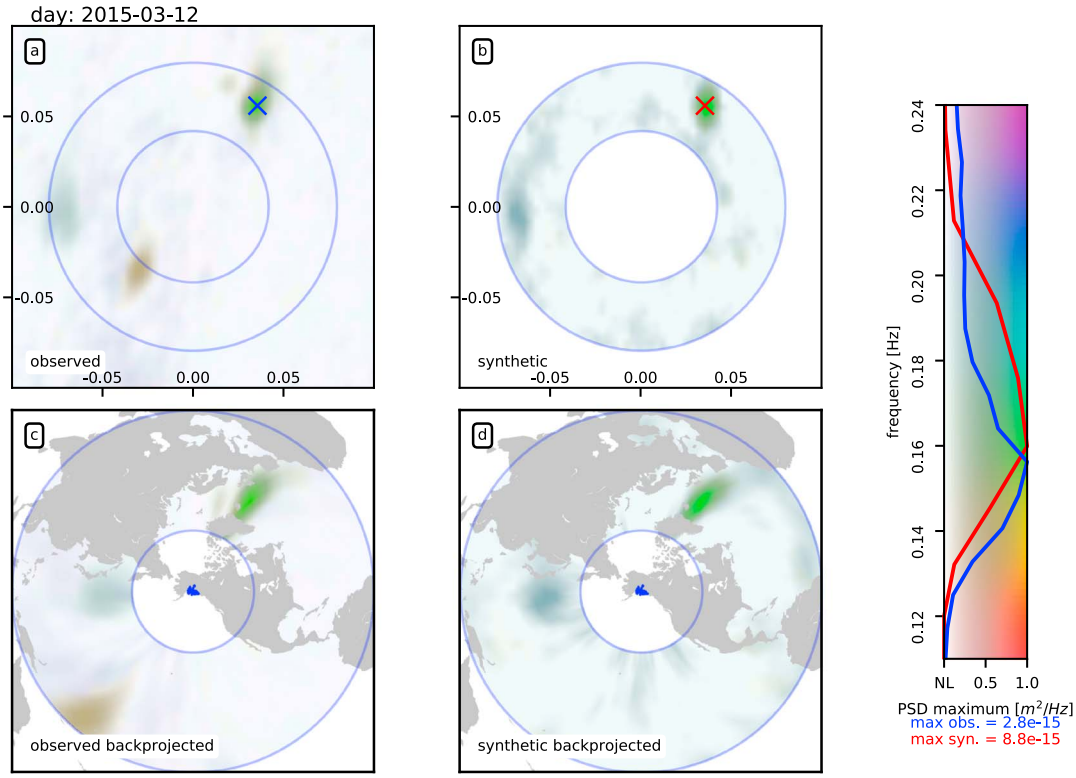

Figure 4. (a and c) Observed and (b and d) synthetic beam PSD at the Alaska array on 12 March 2015. Color hue represents the dominant frequency and color lightness the spectral maximum of the beam PSD (narrow band smoothed). The strongest source with dominant frequency around 0.16 Hz (green) is located south of Greenland, some higher-frequency microseismic energy is generated off the Japanese coast with dominant frequency around 0.20 Hz, and there is a clear observed source with low dominant frequency of 0.13 Hz in the South Pacific. The red and blue spectra in the color bar refer to the strongest source spectra from Figures 4a and 4b that are indicated by a cross.

Figures 4c and 4d show the projection of Figures 4a and 4b on a map, using the *P* wave slowness-distance relation.

The slowness with the highest beam PSD amplitude (from now on *strongest source slowness*) is indicated with a cross in Figures 4a and 4b. We describe the *strongest source PSD*, that is, the PSD that corresponds to the strongest source slowness, by its maximum, called *strongest source amplitude*, and by the frequency of its maximum, called *strongest source frequency*.

The strongest source slowness is nearly the same for B and B_{syn}. In this particular example, *P* wave energy is predominantly emitted by microseisms around Greenland. In addition, weaker sources are observed and modeled north of Japan. A third source in the South Pacific is observed, but it does not appear clearly in the beam PSD of model R.

The observed strongest source amplitude, corresponding to the Greenland source, is with 2.8×10^{-15} m^2/Hz approximately 3.1 times weaker than the predicted one with 8.8×10^{-15} m^2/Hz. The strongest source PSDs are plotted in red and blue in the color bar of Figure 4. The observed (blue) and modeled (red) beam PSD peak around 0.16 Hz, but the observed spectral peak is sharper and better defined. The beam PSD amplitudes of the Japanese source cannot be precisely compared from this plot, but its observed and modeled dominant frequencies of about 0.20 Hz (blue color) are similar. The observed South Pacific source has a low dominant frequency of approximately 0.13 Hz.

Figure 4 shows a case where observed and modeled beam PSD have some similarities but also some differences. We observe the same principal similarities and differences using the California array on the same day.

It is interesting to understand, in particular, why the South Pacific source does not appear in the synthetic beam. Inspection of the input pressure PSD and displacement PSD of the model (not shown) at the position of this source reveals that it does exist and that it corresponds to a tropical cyclone called Pam. However, the amplitudes of pressure PSD and displacement PSD in these regions are so low that this source disappears under the noise level of the much stronger- and higher-frequency sources in Greenland in the final synthetic beam PSD. It is unclear which part of the modeling process is responsible for this mismatch between observed and synthetic beam. The South Pacific source could be too weak, but also the amplitude of the Greenland source, which is clearly overpredicted in model R, raises the noise level of the synthetic beam.

To obtain conclusions about the general quality of the modeling process, we statistically compare observations as the one shown in Figure 4 with the modeled beam PSD in the following sections. Because weaker sources can disappear in the beam PSD behind the noise of significantly stronger ones, as we have seen in the previous example, we concentrate in this article on the strongest sources only that provide the most robust measurements.

3.2. Strongest Sources: Energy Distribution and Geographical Origins

The *strongest source PSD* is the beam PSD at the slowness with the highest beam PSD amplitude, as plotted in the color bar of Figure 4 for a particular day. From all 5 years and arrays we obtain 1,809 strongest source PSDs and slownesses from the observations and equally from each model. Strongest source amplitudes and strongest source frequencies are extracted from the strongest PSDs and describe the amplitude and frequency of their maxima as explained previously. These quantities constitute the observed and corresponding modeled data sets that we analyze and compare in the following sections.

Figure 5a shows the positions of the strongest sources colored by array that observed them. Some jitter (2°) was added to the source positions to better resolve nearby points. Importantly, this plot considers all observed sources to be secondary microseism *P* waves although they could also correspond to some other source of seismic energy such as another body wave phase (e.g., *PP*) or leaked energy from strong surface waves. Many source regions, for example, in the North Pacific, North Atlantic, and South Pacific, are seen individually by several arrays. Others, as at the Pacific coast of South and Central America, can be predominantly seen by one of the arrays.

Some sources can be found on the continents and are certainly not secondary microseism *P* waves. Other observations cluster at the *P* wave observation limits of the arrays, such as around northern South America and the Pacific coast of Central America. Although such sources could be generated by secondary microseisms, they have to be examined with care because they can correspond to energy of a regional phase (for short distances) or a *P* wave that is diffracted around the Earth's core (for large distances). Such signals can leak into the *P* wave slowness range and are not modeled in the synthetic beam. In these two cases, the source distances would be over or underestimated, respectively. In particular, the Mexico and Nevada arrays suffer from higher leakage because they are smaller.

The strongest source density is shown for the observations, model NR, model R, and model NA from Figures 5b–5e. The principal-observed source regions are the northwest Pacific, the South Pacific, the North Atlantic, and the South and Central American Pacific coast. Only model R approximately reproduces all of these source regions. The South and Central American Pacific coast sources do not appear in model NR and are underestimated by model NA, although the latter includes coastal reflections in the same way as model R. Model NA furthermore underestimates the strongest source distribution in the South Pacific and diverges in general most from the observed one.

Many of the observed strongest sources in Figure 5 do not correspond to clean *P* waves from a secondary microseism and cannot be compared to the modeled ones. The strongest sources cannot be impulsive signals such as earthquakes because they were removed in the processing. On the other hand, the strongest sources could correspond to other microseismic body wave phases such as *PP* or to leaked microseismic energy from surface waves. Furthermore, these signals could be generated by unknown, nonmicroseismic processes. Even in the case that an observed strongest source corresponds to a secondary microseism *P* wave, the corresponding modeled strongest source of the same day could be in a completely different region of the Earth.

A comparison can only be made between observed and modeled sources that correspond to each other, that is, that have similar slowness and therefore come from the same position on the same day. Also, sources

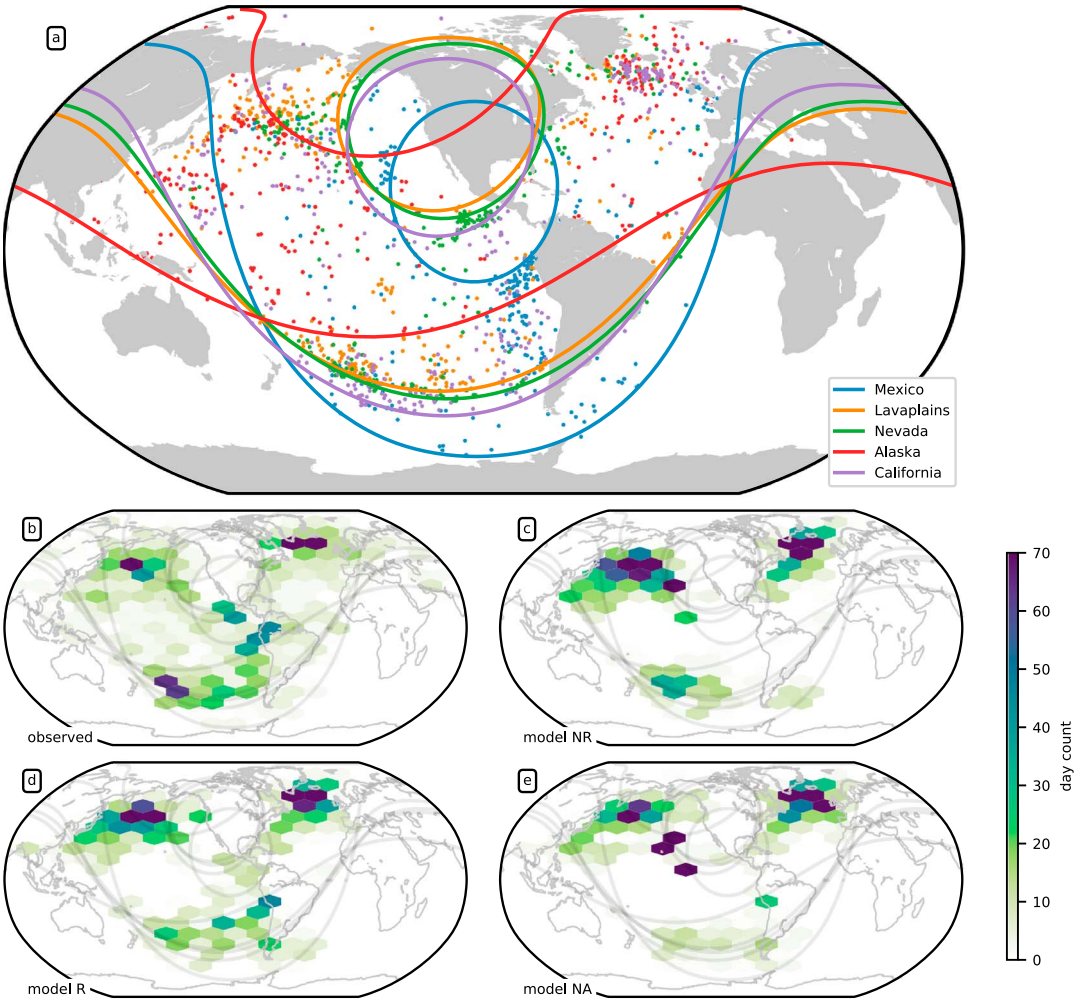

Figure 5. Geographical distribution of the strongest sources. (a) The observed strongest source positions colored by the array that observed them. We have added a small jitter (2°) to the positions to make clusters better visible. Observations that cluster at the observation limits of an array have to be interpreted with caution. (b–e) The source density is shown for observations, model NR, model R, and model NA. The observation limits of the arrays are indicated with lines from Figures 5a and 5e. The observed and modeled source density is biased by the number of arrays that can observe a particular region (see Figure 1b). Model R fits best with the observations. Model NR and NA are missing the coastal reflections along the South American Pacific coast. Model NA has the worst overall fit with the observations.

with a matching modeled counterpart are likely *P* waves from a secondary microseism: It is very unlikely (not impossible) that a signal other than a secondary microseism *P* wave has similar slowness on the same day as the strongest source *P* wave derived from the wind-derived secondary microseism model. Selecting strongest sources with matching modeled counterpart therefore removes observations of other body wave phases, leaked energy, or signals of nonmicroseismic origin. Importantly, this selection mechanism does not imply that we select any a priori strongest source PSD. On the other hand, we do favor source regions that appear in the models, which is necessary for a meaningful spectral comparison.

We therefore call days "matching" with a particular model when the observed and modeled strongest source slownesses on this day are closer than 0.01 s/km (corresponding to a distance of approximately 1,700 km). Otherwise, days are called "nonmatching." The matching days provide us with 469 (model NR), 467 (model R), and 318 (model NA) observed and modeled strongest source PSDs, which correspond to 26% for models NR and R and 18% for model NA of all 1,809 days.

Note that an observed strongest source can be accurately modeled but still be classified as nonmatching. This happens, for example, if another stronger source exists in the model elsewhere which would be selected

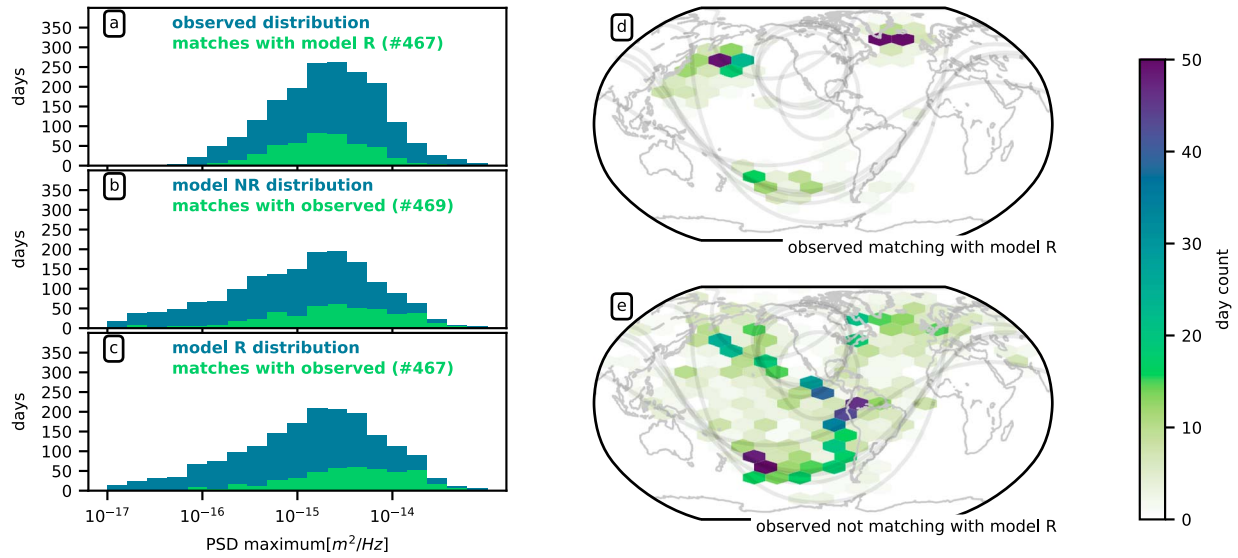

Figure 6. Distribution of the (a) observed, (b) model NR, and (c) model R strongest source amplitudes from all 5 years observed by the five arrays (1,809 total days of observations). Sources are called matching when the observed and modeled strongest sources slowness is similar. The matching source distribution is shown in green and nonmatching sources in blue. (d) The geographical positions of the observed sources that match with model R are concentrated in three dominant source regions: south of Greenland, and in the northwest and South Pacific. (e) The nonmatching source positions also concentrate in these regions but also along the coast of South America. The observation limits of the arrays are indicated in Figures 6d and 6e with faint black lines.

as strongest source. Matching or nonmatching in itself is therefore not a good criterion of the ocean wave model accuracy but a strict data selection procedure that allows us to extract source spectra from the full data set that can be directly compared. It is not our objective to reach the highest number of matching sources but a set of high-quality sources that are very likely to be secondary microseism *P* waves, and that are the least perturbed by other stronger signals. The data set of observed strongest sources matching with model R is shown in detail in Table S1 in the supporting information.

From Table S1, it can be seen that the strongest source spectra have most of the time a single peak. The few more complex spectra that we observe can be the consequence of the limited spatial array resolution that mixes *P* wave energy from a large region or also of perturbations by other signals. This is, in particular, the case for observations from the smaller Mexico and Nevada arrays. During the year 2015, we have many independent observations of the same source from the two North American arrays in California and Alaska (days: 5 January 2015, 7 January 2015, ...). Comparing the spectra of the same source observed by these two arrays (e.g., 5 January 2015) confirms that their strongest source frequencies are in general close and therefore a property of the source rather than a consequence of the observation with a particular array. Some variations in the spectral shape (e.g., 8 January 2015) give an idea of the differences due to observations from different arrays. Many of these differences can be attributed to contamination by strong local noise that influences one array more than another.

Figure 6 shows the full distribution (blue) of the strongest source amplitudes of all 1,809 days corresponding to the observations (a), model NR (b), and model R (c). In each distribution, the portion of strongest sources matching with either model R (a) and the observations (b) and (c) is shown in green.

In contrast to the observed distribution (Figure 6a), the modeled distributions (Figure 6b/6c) have a tail that extends into low amplitudes. This is not surprising, because the observed strongest source PSDs are to some extent biased by noise. The observed distribution (6a) is concentrated more strongly around its center but has a faint high-amplitude tail that does not appear in Figure 6b and only a little bit in Figure 6c.

It is surprising, in Figure 6a, that the observed strongest sources matching with model R (green) have approximately the same distribution as the nonmatching ones (blue). This means that weak observed strongest sources are as likely to have a modeled match as the strong ones. This is different for the modeled distributions

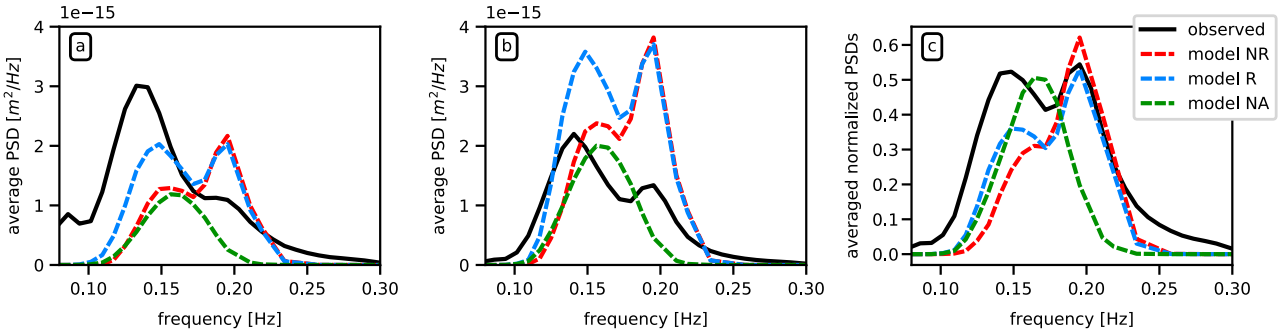

Figure 7. Averages of observed and modeled strongest source PSDs. (a) The average of all strongest source PSDs, (b) the average of the matching strongest source PSDs, and (c) the average of the matching normalized strongest source PSDs (i.e., their maximum is normalized to 1).

(Figure 6b/6c): here clearly the matching strongest sources (green) tend to have higher beam PSD amplitudes than the nonmatching ones (blue). Therefore, strongest sources that are strong in the model are more likely to be observed, as we would expect.

Figure 6 shows maps of the *observed* geographical positions of the strongest sources that match (d) and do not match (e) with model R (corresponding to the distribution in Figure 6a). The matching strongest sources focus in three dominant source regions south of Greenland, in the northwest Pacific and in the South Pacific.

The geographical positions of the observed strongest sources that do not match with model R are widely distributed over the oceans. Less so than the matching sources, they still clearly concentrate in some specific regions, most notably in the north central Pacific, along the South and Central American coastlines, and in the South Pacific. Although some of these nonmatching observations are surely contaminated by noise, their nonrandom regional distribution implies that they are to a large extent also related to secondary microseisms. In particular, the strong concentration of nonmatching sources at the Pacific coast of northern South and Central America is likely caused by leakage from regional *P* waves to the Mexico and Nevada arrays. These arrays are fairly small, and leakage is therefore more prominent. Similarly, some of the nonmatching South Pacific sources might correspond to leakage from *P* or *P*diff phases beyond the 90° distance range.

Figure 7 shows the average of all strongest source PSDs (a), of the matching strongest source PSDs (b), and of the matching normalized strongest source PSDs (i.e., their maximum is normalized to one) (c). The different lines correspond to the observed (black), model NR (red dashed line), model R (blue dashed line), and model NA (green dashed line) averages.

One striking feature of the averaged PSDs in Figures 7a–7c are two distinct spectral peaks that appear in observations and in the models that take into account water column resonance (models NR and R). The first peak is around 0.13–0.15 Hz and the second around 0.19–0.20 Hz. Model NA, which does not take into account the water column resonance, has only a single broad maximum around 0.16–0.17 Hz. Model NA reflects the actual ocean wave pressure PSD, only slightly distorted by seismic propagation effects such as attenuation. The absence of the spectral peaks in model NA indicates that they are a consequence of the resonance effect, caused by the source-site amplification shown in Figure 3.

At low frequency, the averaged strongest source PSD peak in Figure 7a is at about 0.13 Hz in the observations, and not like in model R at 0.14 Hz, in model NR at 0.15 Hz, and in model NA at 0.16 Hz. Another difference is that there is more low-frequency energy in all observed strongest sources than in all modeled sources, whereas the high-frequency energy is weaker in the observation. The averages of all strongest source PSDs give an idea about the strongest source PSDs before selecting matching sources only, but they are not directly comparable because they might correspond to completely different sources.

If we look at the average strongest source PSD of the matching days only, shown in Figure 7b, the observed excess low-frequency energy vanishes. Here the modeled amplitudes are stronger at all frequencies compared to Figure 7a. One reason is that strongest sources with modeled high amplitude are matching more often

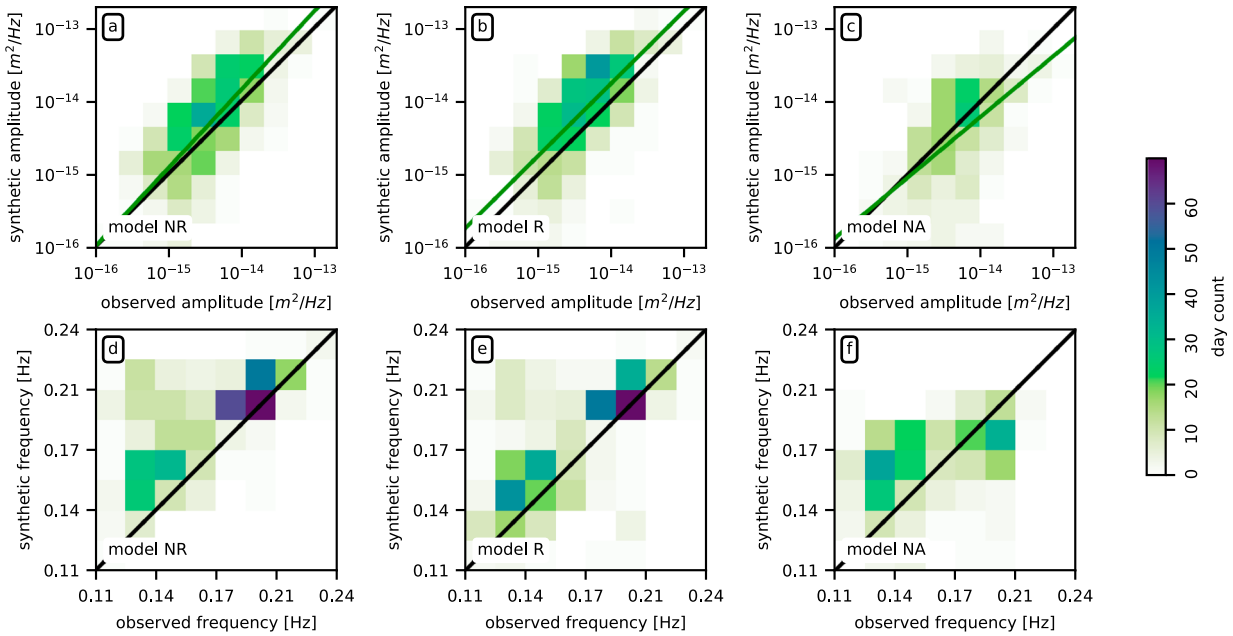

Figure 8. Comparison of matching observed and modeled (a–c) strongest source amplitudes and (d–f) strongest source frequencies from all 5 years and arrays. The observed amplitudes are compared with models NR (Figure 8a), model R (Figure 8b), and model NA (Figure 8c) and the observed frequencies with model NR (Figure 8d), model R (Figure 8e), and model NA (Figure 8f). The lines show equality (black) and a linear least squares fit (green) in log-log space.

with observations (see Figure 6b/6c). The average observed strongest source PSD on the other hand becomes weaker at low frequencies and slightly stronger at high frequencies when only matching sources are used. This means that the nonmatching sources are dominated more strongly by low-frequency energy. It remains unclear from Figures 7a and 7b whether the average strongest source PSDs are mostly influenced by the spectral shape of the ensemble of the sources or due to a few particularly strong ones.

Normalizing the spectra before averaging ensures that all sources contribute in the same way to the average. The average of the matching normalized strongest source PSDs is shown in Figure 7c and shows that there are as many observed low-frequency and high-frequency sources. The models, however, have more high-frequency than low-frequency sources. A comparison with the unnormalized averages in Figure 7b shows that normalization reduces the amplitudes of the low-frequency sources compared to the high-frequency ones. This is a hint that the low-frequency matching sources are in general more energetic than the high-frequency ones in the observations and in the models.

We conclude several things from this section: secondary microseism *P* wave energy concentrates in two spectral peaks, likely because of resonance effects in the source-site water column. The observed strongest sources match in slowness with the modeled ones on about 26% of all days for models NR and R and on about 18% days for model NA. Models NR and R can reasonably well explain the double peak of the averaged matching source spectra. However, the observed low-frequency resonance peak is at slightly lower frequencies than in the models. Also, the modeled matching sources are more often high frequency dominated than the observed ones, and their amplitudes are slightly higher in general. Low-frequency sources are more energetic than the high-frequency sources in observations and models. The site-effect amplification therefore seems important to quantitatively model observed *P* wave spectra.

3.3. Matching Strongest Sources: Energy and Dominant Frequency

Figure 8 shows a comparison of the observed with modeled matching strongest source amplitudes (a–c) and frequencies (d–f) for model NR (a/d), model R (b/e), and model NA (c/f).

The (geometric) average of the strongest source amplitudes is accurately modeled to a factor of 1.3 (Figure 8a), 1.7 (Figure 8b), and 0.70 (Figure 8c). The standard deviations around a linear least squares fit of the logarithmic

strongest source amplitudes correspond to factors of 3.2 (Figure 8a), 3.1 (Figure 8b), and 3.8 (Figure 8c). The matching strongest source amplitudes are therefore roughly predicted within a factor of 0.4–6 by the models NR and R. All models predict the strongest source amplitudes of the matching sources reasonably well. These numbers should be seen in the perspective of ocean wave energy that can vary by multiple orders of magnitude.

Amplitudes tend to be slightly overestimated by models NR (Figure 8a) and R (Figure 8b). Model NR has slightly weaker amplitudes than model R, which adds energy due to coastal reflections, and therefore fits the observed amplitudes a little bit better at low frequencies. The amplitude of model NA also fits approximately the observed values, but it depends on the a priori unit amplitude that we have chosen for the site amplification factor. Note that these details can be independently seen at all arrays and years (see Figure A1).

The strongest source frequency shown in Figures 8d and 8e indicate two principal groups of strongest source PSDs corresponding to the two spectral peaks seen in Figure 7. There is a group of low-frequency sources with dominant frequencies around 0.14 Hz, and there is a group of high-frequency sources with dominant frequencies around 0.20 Hz. These two groups, with a gap in between, are modeled and observed independently in Figures 8d and 8e. For most sources the observed and modeled dominant frequencies belong to the same group and are very close.

The strongest source frequencies (Figure 8f) of model NA do not have this characteristic. Here the synthetic dominant frequencies are distributed smoothly over a smaller interval, while the observed have the characteristic double peak.

Sometimes, model NR (and less so model R) wrongly predicts a source in the high-frequency group when a low-frequency one is observed. The opposite is rarely the case, that is, that a low-frequency source is predicted when a high-frequency source is observed. This is causing the average (Figure 7c) of the matching observed PSDs to have more low-frequency energy than the modeled ones. Including coastal reflections, as in model R shown in Figure 8e, enhances the fit compared to model NR shown in Figure 8d, because it adds low-frequency energy to the source pressure PSD. As we have seen from the average strongest source PSDs (Figures 7b and 7c), the observed low-frequency peak is also at slightly lower frequencies than the modeled one.

Modeled and observed strongest source PSDs fit reasonably well in terms of the amplitudes and frequencies of their maxima. In the following, we examine the full shape of the strongest source PSDs as a function of frequency and associate them with geographical regions.

3.4. Matching Strongest Sources: Cluster Analysis

The existence of different groups of strongest source PSDs with distinct spectral shape suggests that they can potentially be classified in a meaningful way. We can then examine the average spectral shape and geographical distribution of the individual classes instead of averaging over the entire data set. To this end, we use a k-means cluster algorithm (Arthur & Vassilvitskii, 2007; Pedregosa et al., 2011) that extracts representative PSDs from the observations, fully independent from the models. To focus on spectral shape rather than amplitude of the strongest sources, we normalize strongest source PSDs to have unit maximum. We then set the k-means algorithm to compute five mean spectra (called "centroids") that minimize the summed L2 distances between the normalized observed strongest source PSDs and the closest centroid.

Each day can then be labeled with the index #0–#4 of the centroid that the observed strongest source PSD of this day is closest to (Table S1 in the supporting information contains all labels). Importantly, the modeled spectra are labeled according to the centroid that the observed strongest source PSD is closest to, as well. Our data set of matching days is therefore subdivided into the five centroids based purely on the observations. We call the set of observed and modeled beam PSDs that belong to the same centroid a "cluster."

Figure 9a shows the mean observed (black solid) and modeled (red, blue, and green dashed lines) strongest source PSDs of each cluster. For each cluster, the mean is taken over the subset of days, which belong to the same cluster. Because the clusters were computed based on the observations, the mean observed beam PSD of a cluster is the same as its centroid.

The clusters are ordered by the frequency of the maximum of their centroid PSD, that is, by the observed strongest source frequency, from lowest frequency (#0) to highest frequency (#4), as can be seen in Figure 9a.

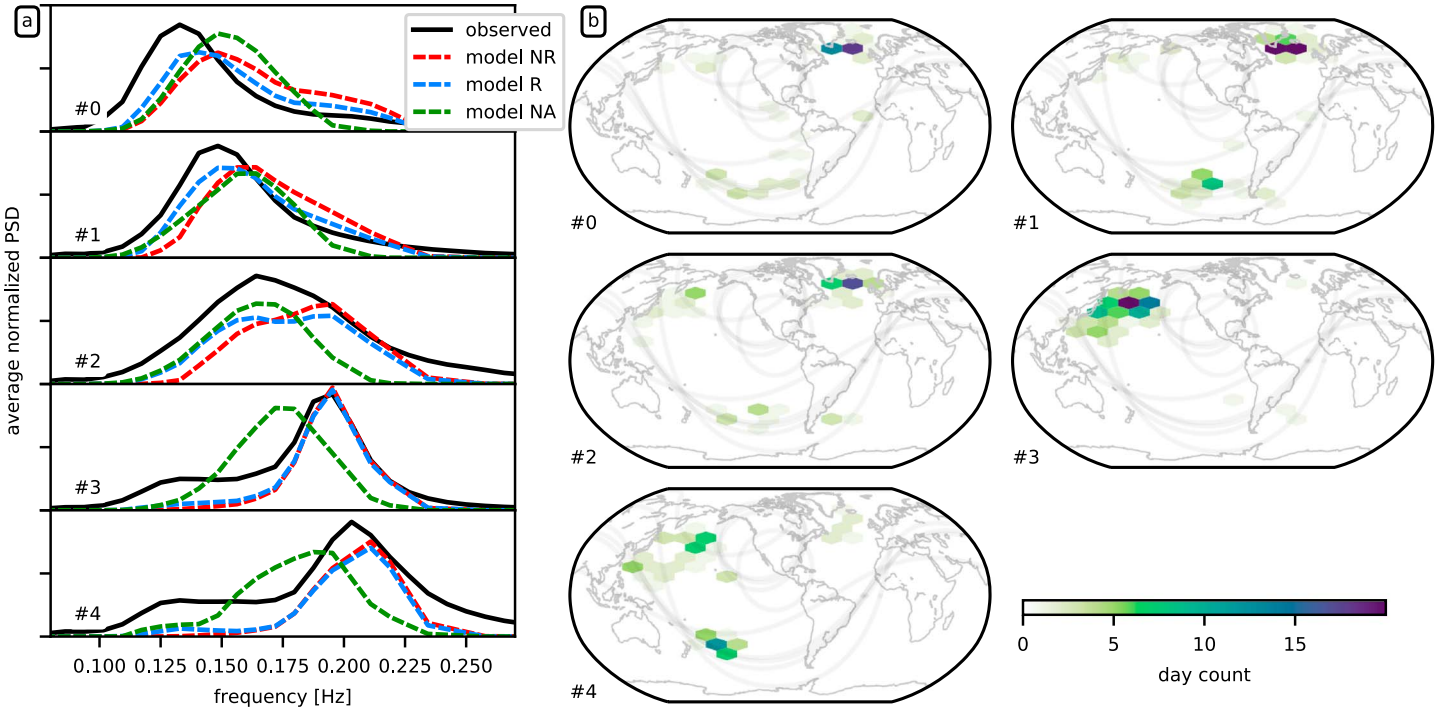

Figure 9. (a) Centroid beam PSDs (black) #0–#4 that divide the data set of matching normalized sources into five different groups. Red, blue, and green are the modeled beam PSDs averaged over the members of a particular cluster. They are ordered from lowest to highest dominant frequency. (b) Spatial distribution of clusters #0–#4. The observation limits of the arrays are indicated in Figure 9b with faint black lines.

The centroid PSDs #0 and #1 have a low-frequency peak at 0.13 Hz (7.7 s) and 0.15 Hz (6.7 s), respectively. Centroid PSD #2 has a broad intermediate peak between 0.16 Hz (6.7s) and 0.18 Hz (5.5 s), and the centroid PSDs #3 and #4 have a high-frequency peak at 0.18 Hz (5.5 s) and 0.21 Hz (4.8 s), respectively. Clusters #0 and #1 can therefore be seen as low-frequency-dominated sources, and #3 and #4 as high-frequency ones. Cluster #2 covers the intermediate frequency range.

Figure 9b shows maps of the spatial distribution of these clusters from #0 to #4, that is, histograms of the number of observations that correspond to each cluster. The number of observations is biased by the coverage of the globe by the five arrays but also by the quality of the arrays that were used in this article. The spatial distribution of the clusters allows the identification of spectral characteristics of particular regions.

The source region at the Greenland coast contains mostly low frequency sources of type #0–#2, predominantly of type #1. Other regions with mostly low frequency sources of type #1 are in the south central Pacific over the East Pacific Rise. The low-frequency south central Pacific sources are particularly interesting because the centroid dominant frequency (0.15 Hz) of cluster #1 corresponds to typical ridge depth resonance frequencies (see Figure 3).

The low-frequency centroids are not modeled satisfactory, which is what we already observed in Figures 7 and 8. All modeled low-frequency PSDs from clusters #0–#1 have significant high-frequency energy around 0.20 Hz, contrasting with the observed ones. The low-frequency peaks of the observed centroid PSDs in #0 and #1 have slightly lower frequency than the modeled ones. These differences are smaller for model R that fits the centroid PSDs #0 and #1 better than model NR.

High-frequency source #3 can mostly be found in the northeast Pacific along and north of the Japanese coast. This source region can be associated with typhoons that move from south to north along the coast. They emit *P* waves with a characteristic high-frequency-dominated spectrum. Source type #4 can also be found in this region but also in the western South Pacific.

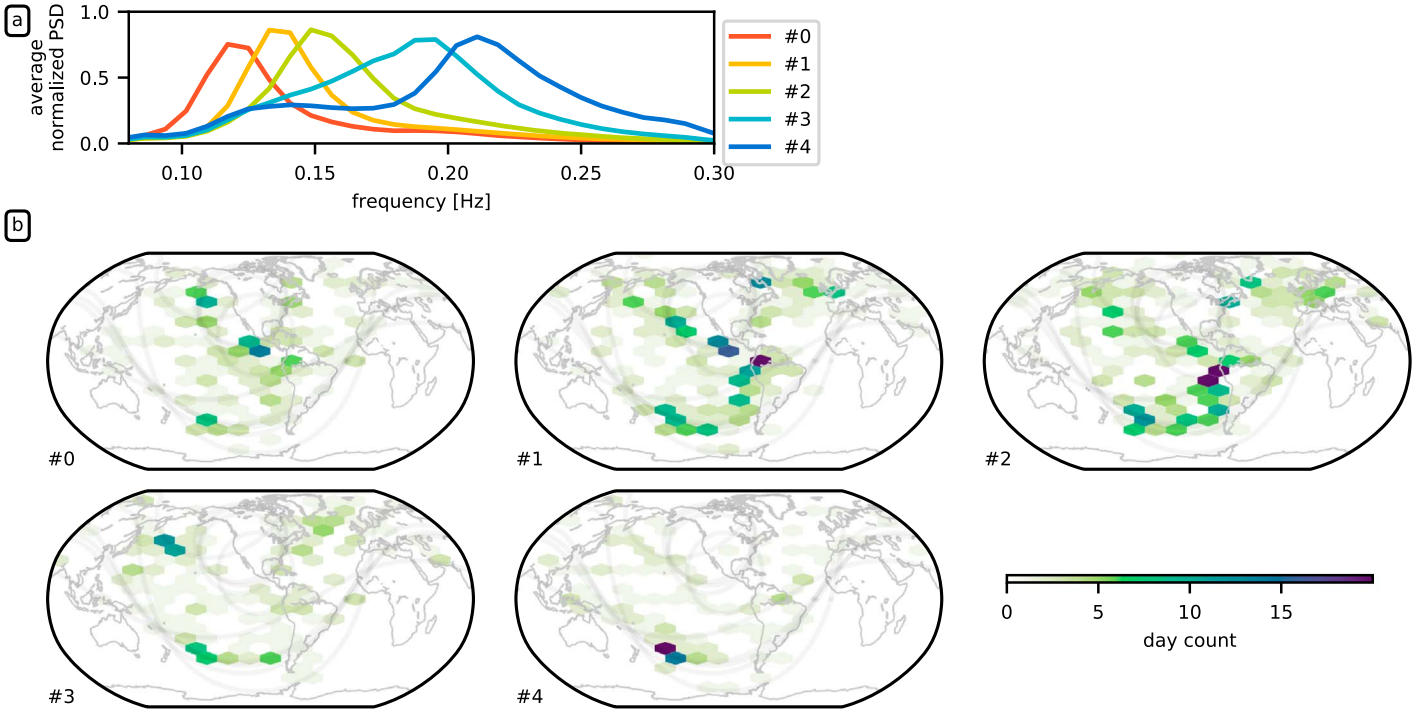

Figure 10. (a) Centroid beam PSDs #0–#4 that divide the data set of nonmatching normalized strongest sources into five different groups. They are ordered from lowest to highest dominant frequency. (b) Spatial distribution of clusters #0–#4. The observation limits of the arrays are indicated in Figure 10b with faint black lines.

In contrast to the low-frequency ones, high-frequency sources are modeled quite accurately, in particular, for cluster #3. The observed high-frequency peak around 0.20 Hz due to the source-site resonance frequency is modeled very accurately. The peak width of centroid PSD #3 is less wide than the peak width of centroid PSDs #0 and #1. This behavior is reproduced in the models and is a consequence of the varying width of the resonance peaks (see Figure 3a). The spectral peak of the centroid PSD #4 is not as narrow as the one of centroid PSD #3, possibly because these sources are not as homogeneous in spectral shape as cluster #3 sources. Also, in the high-frequency clusters, observed low-frequency energy is stronger than the modeled one.

3.5. Nonmatching Strongest Sources: Cluster Analysis

Finally, we also subdivide the nonmatching observed sources (using the same approach as for the matching sources) to find five centroid spectra that minimize the L2 distance to the full data set of nonmatching normalized spectra. In this case, we cannot compare the observed and the modeled spectra because their slowness is associated with a different source region. Note that a notable part of these sources might correspond to other signals than secondary microseism *P* waves, as we have explained previously. Therefore, they have to be interpreted with care.

The cluster centroids shown in Figure 10a are again ordered from lowest to highest dominant frequency. They split into a group of low-frequency (#0–#2 from 0.12 to 0.16 Hz) and high-frequency (#3-#4 from 0.19 to 0.22 Hz) clusters, again confirming that there are only few spectra with dominant frequency around 0.17 Hz.

The spatial distribution of the clusters (Figure 10b) shows a large group of low-frequency sources along the Central and South American Pacific coast (#0–#2), with a particular high concentration at the northwestern tip of South America. Another accumulation of nonmatching low-frequency sources can be seen in the central Pacific. As we have argued before, a large part of these sources cluster at the *P* wave observation limits of the Mexico and Nevada arrays that suffer from high leakage in slowness domain. In our experience, a large part of these phases corresponds to regional *P* waves from sources closer than 30° that leak into the *P* wave

slowness range. They might therefore correspond to secondary microseisms but are not mapped accurately and are not well modeled by ray theory.

Many low- and high-frequency sources are also located in the South Pacific. Here the low-frequency sources are spread from east to west over the South Pacific but the high-frequency sources are concentrated in the west. Again, these sources concentrate around the *P* wave observation limits of the arrays and likely correspond to *P* waves that become influenced by the Earth's core from sources at larger distances than 90°.

4. Discussion

Our analysis of secondary microseismic *P* waves confirms source regions that have been seen and studied by many authors.

The North Atlantic, around Greenland, is known to have strong microseismic activity over the whole year and has been studied using surface and body waves (e.g., Euler et al., 2014; Kedar et al., 2008; Landès et al., 2010; Liu et al., 2016; Nishida & Takagi, 2016; Obrebski et al., 2013; Sergeant et al., 2013; Stehly et al., 2006; Stutzmann et al., 2012). Microseismic sources from the northwest Pacific have also been studied in detail using different seismic phases and arrays (e.g., Farra et al., 2016; Gal et al., 2015; Landès et al., 2010; Obrebski et al., 2013; Pyle et al., 2015; Zhang, Gerstoft, & Bromirski, 2010), and—although the Southern Hemisphere is less well studied—a number of studies identified sources in the South Pacific, east of Australia (Euler et al., 2014; Gal et al., 2015; Landès et al., 2010; Reading et al., 2014).

To our knowledge, there are no studies of the coastal sources that we have observed along the Pacific coast of Central and South America. Further examination of these sources would be particularly interesting, because they seem to be most strongly related to coastal reflections (compare Figure 5d with Figure 5c) and therefore allow to isolate this phenomenon.

Contrary to the abundance of studies on source location, few authors examined the spectral characteristics of secondary microseismic sources. Many studies average over frequency bands that are too large to see the spectral source characteristics that we have observed. However, a general dependence of source location on frequency is a common observation (e.g., Euler et al., 2014; Gal et al., 2015; Zhang et al., 2009).

Cluster analysis, as shown in this article, allows to separate observed sources with different spectra automatically and to associate them with different regions. Our two data sets, one with matching modeled sources and one without matching modeled sources, are divided into characteristic low-frequency and high-frequency clusters.

Several observations of dominant microseismic *P* wave frequencies from North Pacific sources have been reported at 0.20 Hz (Farra et al., 2016; Obrebski et al., 2013; Neale et al., 2017; Zhang, Gerstoft, & Bromirski, 2010). In our matching strongest sources data set these corresponds to cluster #3 sources that are located in the deep North Pacific as well. A strong *P* wave source around Greenland has been seen with dominant frequency of approximately 0.13 Hz (Nishida & Takagi, 2016), corresponding to cluster #0 that we have also found to be concentrated in the same region.

These independent observations of similar dominant frequencies in similar regions support our conclusion that the dominant frequency of secondary microseism *P* waves is to a large extent controlled by the source region. As we have shown, this can be explained and quantitatively modeled as the consequence of source-site resonance as formulated by Ardhuin and Herbers (2013), Gualtieri et al. (2014), and Farra et al. (2016).

Importantly, source-site resonance, and therefore water depth, seems to have a stronger influence on the dominant frequency than the variations of the pressure source spectrum induced by wave-wave interactions. Figure 11a shows the relation between matching strongest source frequency and the ocean height at their geographical position. We have used a bathymetry map smoothed over a spherical cap with radius of ∼5° to extract the ocean height. Due to the limited resolution of the strongest source position, this is only an approximate depth.

As explained by equation (6), the shallow water peak corresponds to the first harmonic and the deep water peak to the second harmonic of *P* wave resonance in the water column, shown in Figure 11a with black lines. The average PSDs of the matching strongest sources are shown in Figure 11b. The PSD double peak

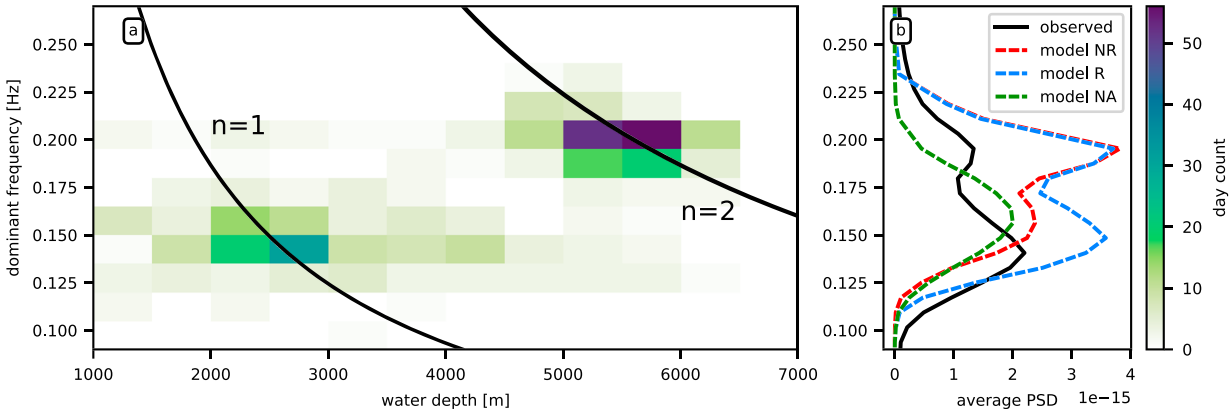

Figure 11. (a) Comparison of observed dominant frequency and water depth at the observed geographical origin of the matching strongest sources. The resonance frequencies for slownesses in the 30° – 90° distance range (takeoff angles of 3.5° – 7.9°) are shown with black lines. (b) The average PSDs of observations and models. Comparing with Figure 11a, it becomes evident that the two peaks are a combined effect of the wave energy distribution (see model NA in Figure 11b) and the water column resonance frequencies.

in the observations and in the models NR and R lies at frequencies where the pressure PSD source, exemplified by model NA, is amplified by resonance.

Although several articles have modeled secondary microseism surface wave spectra at isolated stations (e.g., Ardhuin et al., 2011; Kedar et al., 2008; Stutzmann et al., 2012), synthetic secondary microseism *P* wave spectra are yet uncommon. Neale et al. (2017) computed synthetic *P* wave beam energy using an empirical regression formalism, whereas Farra et al. (2016) and Nishida and Takagi (2016) used wave propagation theory to compute synthetic beams, as we did in this article.

The results of this article show that at least for the matching strongest sources, modeled (models NR and R) and observed beam PSDs are quite similar. Model R predicts the spectral shape better, in particular, because it adds low-frequency energy to the *P* wave spectra compared to model NR. Also, the general strongest source distribution of model R is more similar to the observed one, in particular, along the Pacific coast of South and Central America. However, model R cannot reconcile all the differences of model NR with observations. Model NA does not correctly predict the observed spectral characteristics. The remaining differences between model R and the observations can be attributed to four principal causes: (i) the ocean wave model could be inaccurate; (ii) our model of Earth's structure, in particular, under the source (ocean bottom) and under the array could be inaccurate; (iii) the plane wave assumption and ray theory that are used to compute the synthetic beam PSD have limitations; and (iv) unmodeled signals add noise to the observations.

Apart from inaccuracies in the ocean wave model, which are difficult to estimate here, we expect heterogeneous Earth structure to be responsible for the largest part of the discrepancies between observed and modeled beams: Wavefronts are distorted by seismic heterogeneities, which lowers their coherence and therefore the beam PSD amplitude. *P* wave travel time residuals among stations of an array are expected to be smaller than 1 s (Zhang, Gerstoft, & Shearer, 2010), so that the observed beam amplitude should be reduced by less than 20%. Furthermore, we have used a two-layer model with basaltic material under the ocean bottom to compute the amplification factor. This assumption may not be valid everywhere. Assuming a two-layer model with sediment material under the ocean bottom, can greatly reduce the resonance amplification to very low values, as, for example, from a factor of 3.7 to 2.2 for soft sediments (parameters extracted from model Crust 1.0 (Laske et al., 2013): $\rho_{\text{solid}} = 2,300$ kg/m^3, $\beta_{\text{solid}} = 2,000$ m/s, and $\alpha_{\text{solid}} = 3,300$ m/s). Additional resonances within the sediment layer are also likely, which requires taking into account a realistic multilayer medium under the ocean. Such a model has the potential to reconcile part of the differences that we have observed, in particular, the mismatch of the observed and modeled low-frequency peaks. Sediments have been empirically associated with variations in microseism amplitude (Liu et al., 2016; Nishida & Takagi, 2016), and a detailed treatment will be necessary in future studies to improve our knowledge of the modeling error.

Much information is contained in the nonmatching sources that were not used for comparison with the models in this article. Neale et al. (2017) were able to find 90% of matching observations focusing on the North Pacific only and excluding noisy observations beforehand. We think the selection rate of 26% of all days that we were able to use is much lower because of the following:

1. Secondary maxima are not compared in our data set. When multiple strong sources exist, the models can easily predict a different strongest source region than observed. Even days with small mismatches between models and observation can therefore be classified as nonmatching. Given the range of source amplitudes (see Figure 6), this can easily occur. A better selection criterion than the strongest daily source has the potential to provide a much larger data set, which could, for example, allow one to compare the nonmatching coastal sources to the models. On the other hand, the big advantage of using the strongest source only is that its beam PSD is least perturbed by other sources.
2. Noisy observations are included in our data set. The median criterion that we have used can only remove outliers *within* a day but not a whole day that is noisy due to, for example, a very large earthquake or local noise. A typical example would be a local storm that generates surface waves that raise the noise level high enough to mask secondary microseism *P* waves at any slowness. On such a day, the strongest source does not correspond to a secondary microseism but to a random fluctuation of leaked surface wave energy and will very likely end up in the nonmatching data set.
3. We locate observed sources from the maximum of the narrowband smoothed PSD (0.04 Hz). We were able to increase our data set to 35% of all days using the broadband smoothed PSD (width of about 0.1 Hz). A plausible explanation for this is that uncorrelated noise is reduced by averaging over a larger band, whereas the correlated signal is retained. A broadband only match is therefore an indicator for a noisy observation, which is why we have decided against using them.

5. Conclusions

We have characterized spectra (beam power spectral densities) of *P* waves that were generated by secondary microseisms. We compiled a database of spectra that we analyzed in terms of amplitude, dominant frequency, and geographical origin by systematic extraction of the strongest daily microseismic source from 5 years of vertical component data recorded by five North American arrays. We compared our observed spectra with synthetic data sets that were computed using an ocean wave hindcast (Ardhuin et al., 2011) and the formalism developed by Farra et al. (2016).

The dominant frequencies of the observed *P* wave spectra are concentrated in two distinct frequency bands, either around 0.13–0.15 Hz or 0.19–0.21 Hz, forming two spectral peaks. The sources can be classified by spectral shape using cluster analysis: low-frequency clusters (0.13–0.15 Hz) are predominantly detected in the North Atlantic, in the north central and in the southern Pacific, and along the South and Central American Pacific coast. High-frequency clusters (0.19–0.21 Hz) are mostly detected in deep ocean areas as in the northwestern Pacific and the southern Pacific away from the East Pacific Rise.

Modeled sources that match with an observed source in time and location can be found mostly in the North Atlantic, and in the northwestern and South Pacific. Observed sources in the central Pacific and along the Central and South American Pacific coast do not have matching strongest source counterparts in the model. These sources may exist in the model but not as strongest source of the day.

Amplitudes of the matching strongest sources are predicted within a factor of 0.4–6 by the models. Dominant frequencies are also accurately predicted and turn out to be strongly influenced by the resonance frequency of the source-site water column. Water column resonance at ocean depths of about 2,000–3,000 m (shallow ocean) corresponds to the first harmonic with dominant frequencies of about 0.13–0.15 Hz, whereas resonance at ocean depths of about 5,000–6,000 m (deep ocean) corresponds to the second harmonic and leads to dominant frequencies of about 0.20 Hz.

The amplitude of secondary microseism *P* waves depends on the combined strength of ocean wave interactions and source-site resonance. Both determine the principal source regions and spectral characteristics.

The accuracy of quantitative modeling of secondary microseisms is now sufficiently high to allow using standard inversion techniques to extract information about the secondary microseism sources and the subsurface.

Appendix A: Scatterplots for Individual Arrays

This appendix shows a comparison of the matching observed and synthetic (model R) strongest source amplitudes (Figure A1) and frequencies (Figure A2) for each of the five arrays individually. Although each array observes slightly different sources, the overall observation of a spectral double peak, as well as the approximately valid amplitudes in the modeling process, can be seen at each array.

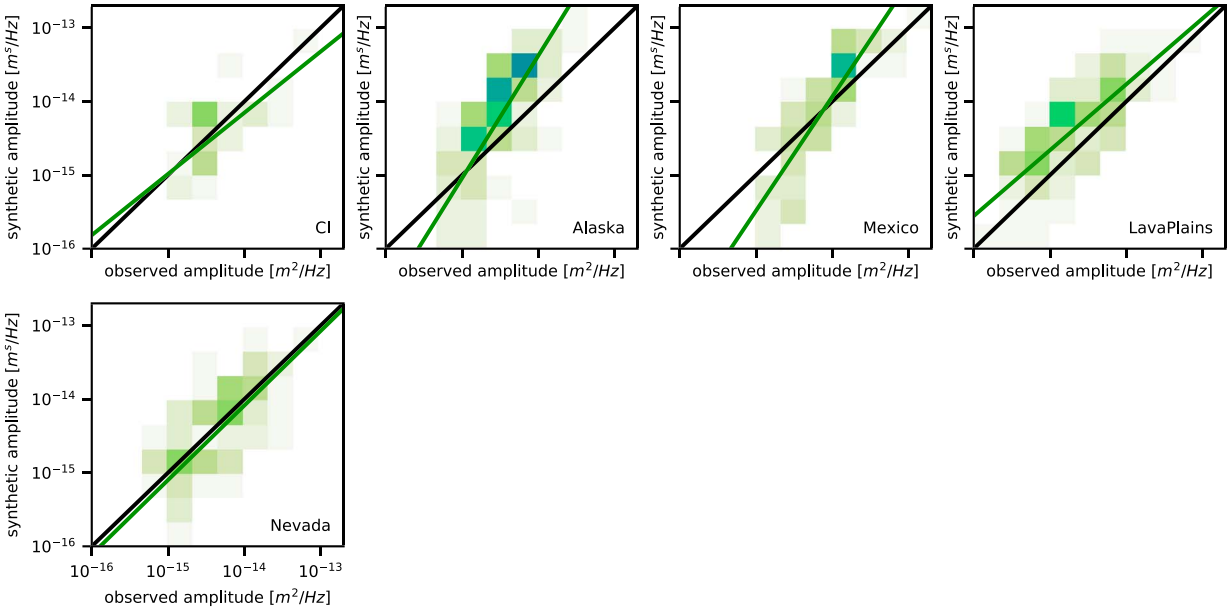

Figure A1. Comparison of the matching observed strongest source amplitudes with model R for arrays (a) CI, (b) Alaska, (c) Mexico, (d) LavaPlains, and (e) Nevada.

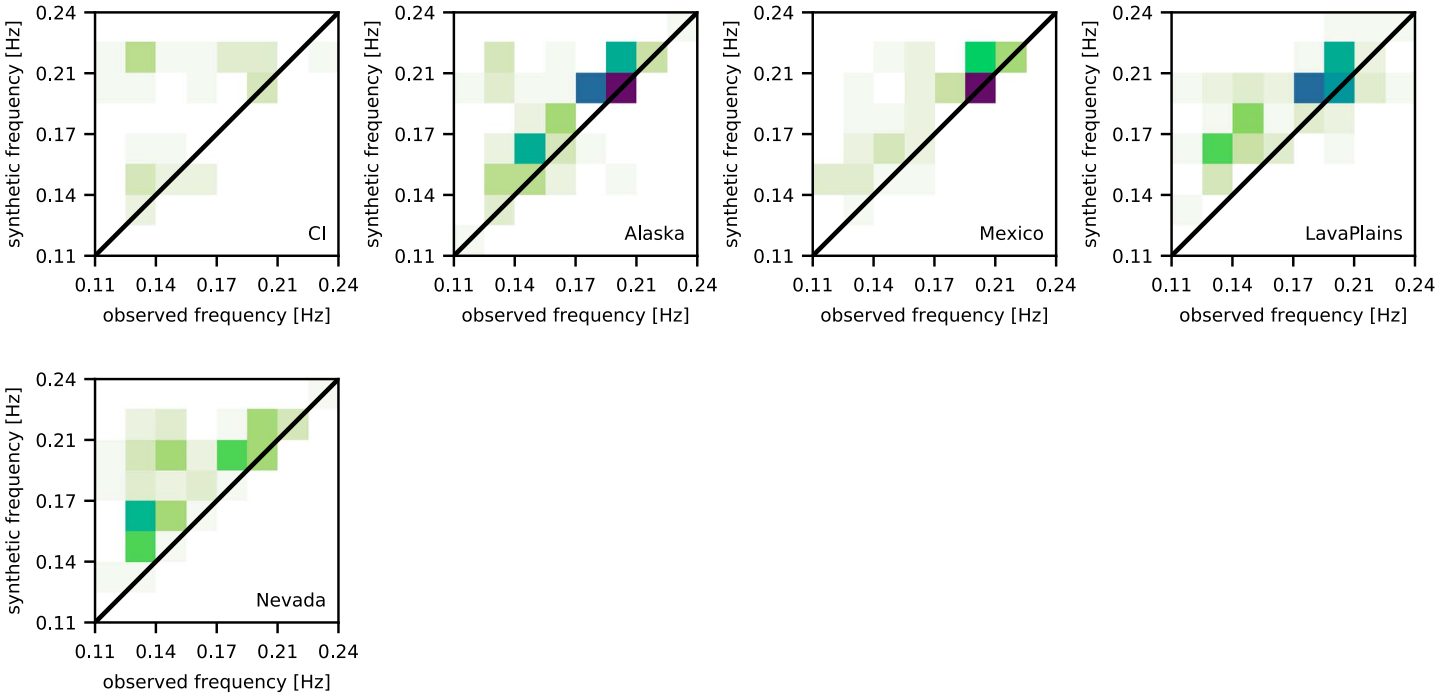

Figure A2. Comparison of the matching observed strongest source frequencies with model R for arrays (a) CI, (b) Alaska, (c) Mexico, (d) LavaPlains, and (e) Nevada.

Acknowledgments
This article was funded through the ANR (Agence National de Recherche) project ANR-14-CE01-0012. The following open scientific software packages were used: obspy (Krischer et al., 2015), numpy and scipy (van der Walt et al., 2011), scikitlearn (Pedregosa et al., 2011), and matplotlib (Hunter, 2007). Numerical computations were performed on the S-CAPAD platform, IPGP, France. The facilities of IRIS Data Services, and specifically the IRIS Data Management Center, were used in this study for access to waveforms and related metadata from the following seismic networks: AK (Alaska Earthquake Center & Univ. of Alaska Fairbanks, 1987), TA (IRIS Transportable Array, 2003), AT (NOAA National Oceanic and Atmospheric Administration (USA), 1967), CI (California Institute of Technology (Caltech), 1926), ZA (West, 2006), XF (Grand & Ni, 2006), XC (James & Fouch, 2006), and YX (Klemperer & Miller, 2010). IRIS Data Services are funded through the Seismological Facilities for the Advancement of Geoscience and EarthScope (SAGE) Proposal of the National Science Foundation under Cooperative Agreement EAR-1261681. The secondary microseism pressure model with and without coastal reflections was developed as part of the IOWAGA project (ERC grant 240009). It is freely available from Ifremer (ftp://ftp.ifremer.fr/ifremer/ww3/HINDCAST/SISMO/). M. S. acknowledges MISTERIOS (CGL2013-48601-C2-1-R).

References

Alaska Earthquake Center, & Univ. of Alaska Fairbanks (1987). Alaska regional network. Seismic Network. https://doi.org/10.7914/SN/AK

Ardhuin, F., & Herbers, T. H. (2013). Noise generation in the solid Earth, oceans and atmosphere, from nonlinear interacting surface gravity waves in finite depth. *Journal of Fluid Mechanics*, *716*, 316–348.

Ardhuin, F., Stutzmann, E., Schimmel, M., & Mangeney, A. (2011). Ocean wave sources of seismic noise. *Journal of Geophysical Research*, *116*, C09004. https://doi.org/10.1029/2011JC006952

Arthur, D., & Vassilvitskii, S. (2007). k-means++: The advantages of careful seeding. *Proceedings of the Eighteenth Annual ACM-SIAM Symposium on Discrete Algorithms* (pp. 1027–1035). Society for Industrial and Applied Mathematics.

Bertelli, T. (1872). *Osservazioni sui piccoli movimenti dei pendoli in relazione ad alcuni fenomeni meteorologici del pd Timoteo Bertelli barnabita*, Tip. delle scienze matematiche e fisiche.

California Institute of Technology (Caltech) (1926). Southern California seismic network, Other/Seismic Network. https://doi.org/10.7914/SN/CI

Ebeling, C. W. (2012). Inferring ocean storm characteristics from ambient seismic noise: A historical perspective. *Advances in Geophysics*, *53*, 1–33.

Euler, G. G., Wiens, D. A., & Nyblade, A. A. (2014). Evidence for bathymetric control on the distribution of body wave microseism sources from temporary seismic arrays in Africa. *Geophysical Journal International*, *197*, 1869–1883. https://doi.org/10.1093/gji/ggu105

Farra, V., Stutzmann, E., Gualtieri, L., Schimmel, M., & Ardhuin, F. (2016). Ray-theoretical modeling of secondary microseism *P* waves. *Geophysical Journal International*, *206*(3), 1730–1739.

Friedrich, A., Krüger, F., & Klinge, K. (1998). Ocean-generated microseismic noise located with the Gräfenberg array. *Journal of Seismology*, *2*(1), 47–64.

Gal, M., Reading, A., Ellingsen, S., Gualtieri, L., Koper, K. D., Burlacu, R., … Hemer, M. (2015). The frequency dependence and locations of short-period microseisms generated in the Southern Ocean and West Pacific. *Journal of Geophysical Research: Solid Earth*, *120*, 5764–5781. https://doi.org/10.1002/2015JB012210

Gerstoft, P., Sabra, K. G., Roux, P., Kuperman, W., & Fehler, M. C. (2006). Green's functions extraction and surface-wave tomography from microseisms in Southern California. *Geophysics*, *71*(4), SI23–SI31.

Gerstoft, P., Shearer, P. M., Harmon, N., & Zhang, J. (2008). Global *P*, *PP*, and *PKP* wave microseisms observed from distant storms. *Geophysical Research Letters*, *35*, L23306. https://doi.org/10.1029/2008GL036111

Grand, S., & Ni, J. (2006). Mapping the Rivera Subduction Zone, Other/Seismic Network. https://doi.org/10.7914/SN/XF_2006

Gualtieri, L., Stutzmann, E., Farra, V., Capdeville, Y., Schimmel, M., Ardhuin, F., & Morelli, A. (2014). Modelling the ocean site effect on seismic noise body waves. *Geophysical Journal International*, *197*, 1096–1106.

Hadziioannou, C., Gaebler, P., Schreiber, U., Wassermann, J., & Igel, H. (2012). Examining ambient noise using colocated measurements of rotational and translational motion. *Journal of Seismology*, *16*(4), 787–796.

Hasselmann, K. (1963). A statistical analysis of the generation of microseisms. *Reviews of Geophysics*, *1*(2), 177–210.

Haubrich, R. A., & McCamy, K. (1969). Microseisms: Coastal and pelagic sources. *Reviews of Geophysics*, *7*(3), 539–571.

Hunter, J. D. (2007). Matplotlib: A 2D graphics environment. *Computing in Science and Engineering*, *9*(3), 90–95.

IRIS Transportable Array (2003). Usarray transportable array, Other/Seismic Network. https://doi.org/10.7914/SN/TA

James, D., & Fouch, M. (2006). Collaborative research: Understanding the causes of continental intraplate tectonomagmatism: A case study in the Pacific Northwest, other/seismic network. https://doi.org/10.7914/SN/XC_2006

Kedar, S., Longuet-Higgins, M., Webb, F., Graham, N., Clayton, R., & Jones, C. (2008). The origin of deep ocean microseisms in the North Atlantic Ocean. *Proceedings of the Royal Society of London A: Mathematical, Physical and Engineering Sciences* (Vol. 464, pp. 777–793). The Royal Society.

Kennett, B., & Engdahl, E. (1991). Traveltimes for global earthquake location and phase identification. *Geophysical Journal International*, *105*(2), 429–465.

Klemperer, S., & Miller, K. (2010). Collaborative research: 4D multi-disciplinary investigation of highly variable crustal response to continental extension in the north-central basin and range, other/seismic network. https://doi.org/10.7914/SN/YX_2010

Koper, K. D., De Foy, B., & Benz, H. (2009). Composition and variation of noise recorded at the Yellowknife Seismic Array, 1991–2007. *Journal of Geophysical Research*, *114*, B10310. https://doi.org/10.1029/2009JB006307

Koper, K. D., Seats, K., & Benz, H. (2010). On the composition of Earth's short-period seismic noise field. *Bulletin of the Seismological Society of America*, *100*(2), 606–617. https://doi.org/10.1785/0120090120

Krischer, L., Megies, T., Barsch, R., Beyreuther, M., Lecocq, T., Caudron, C., & Wassermann, J. (2015). ObsPy: A bridge for seismology into the scientific Python ecosystem. *Computational Science & Discovery*, *8*(1), 14,003.

Laske, G, Masters, G., Ma, Z., & Pasyanos, M. (2013). Update on CRUST1. 0–A 1-degree global model of Earth's crust. *Geophysical Research Abstracts*, *15*, EGU2013–2658.

Landès, M., Hubans, F., Shapiro, N. M., Paul, A., & Campillo, M. (2010). Origin of deep ocean microseisms by using teleseismic body waves. *Journal of Geophysical Research*, *115*, B05302. https://doi.org/10.1029/2009JB006918

Liu, Q., Koper, K. D., Burlacu, R., Ni, S., Wang, F., Zou, C., … Reading, A. M. (2016). Source locations of teleseismic *P*, *SV*, and *SH* waves observed in microseisms recorded by a large aperture seismic array in China. *Earth and Planetary Science Letters*, *449*, 39–47.

Longuet-Higgins, M. S. (1950). A theory of the origin of microseisms. *Philosophical Transactions of the Royal Society of London A: Mathematical, Physical and Engineering Sciences*, *243*(857), 1–35.

Meschede, M., & Stutzmann, E. (2016). Colormap2d-v0.5, Other/Python Package. https://doi.org/10.5281/zenodo.192611

Montagner, J.-P., & Kennett, B. (1996). How to reconcile body-wave and normal-mode reference earth models. *Geophysical Journal International*, *125*(1), 229–248.

Neale, J., Harmon, N., & Srokosz, M. (2017). Monitoring remote ocean waves using *P*-wave microseisms. *Journal of Geophysical Research: Oceans*, *122*, 470–483. https://doi.org/10.1002/2016JC012183

Nishida, K., & Takagi, R. (2016). Teleseismic *S* wave microseisms. *Science*, *353*(6302), 919–921.

Nishida, K., Kawakatsu, H., Fukao, Y., & Obara, K. (2008). Background Love and Rayleigh waves simultaneously generated at the Pacific Ocean floors. *Geophysical Research Letters*, *35*, L16307. https://doi.org/10.1029/2008GL034753

NOAA National Oceanic and Atmospheric Administration (USA) (1967). National tsunami warning center Alaska seismic network, Other/Seismic Network. https://doi.org/10.7914/SN/AT

Obrebski, M., Ardhuin, F., Stutzmann, E., & Schimmel, M. (2013). Detection of microseismic compressional (*P*) body waves aided by numerical modeling of oceanic noise sources. *Journal of Geophysical Research: Solid Earth*, *118*, 4312–4324. https://doi.org/10.1002/jgrb.50233

Pedregosa, F., Varoquaux, G., Gramfort, A., Michel, V., Thirion, B., Grisel, O., … Duchesnay, É. (2011). Scikit-learn: Machine learning in python. *Journal of Machine Learning Research*, *12*, 2825–2830.

Pyle, M. L., Koper, K. D., Euler, G. G., & Burlacu, R. (2015). Location of high-frequency *P* wave microseismic noise in the Pacific Ocean using multiple small aperture arrays. *Geophysical Research Letters*, *42*, 2700–2708. https://doi.org/10.1002/2015GL063530

Rascle, N., & Ardhuin, F. (2013). A global wave parameter database for geophysical applications. Part 2: Model validation with improved source term parameterization. *Ocean Modelling*, *70*, 174–188.

Reading, A. M., Koper, K. D., Gal, M., Graham, L. S., Tkalčić, H., & Hemer, M. A. (2014). Dominant seismic noise sources in the Southern Ocean and West Pacific, 2000–2012, recorded at the Warramunga Seismic Array, Australia. *Geophysical Research Letters*, *41*, 3455–3463. https://doi.org/10.1002/2014GL060073

Rost, S., & Thomas, C. (2002). Array seismology: Methods and applications. *Reviews of Geophysics*, *40*(3), 1008. https://doi.org/10.1029/2000RG000100

Schimmel, M., & Gallart, J. (2007). Frequency-dependent phase coherence for noise suppression in seismic array data. *Journal of Geophysical Research*, *112*, B04303. https://doi.org/10.1029/2006JB004680

Schimmel, M., & Paulssen, H. (1997). Noise reduction and detection of weak, coherent signals through phase-weighted stacks. *Geophysical Journal International*, *130*(2), 497–505.

Schimmel, M., Stutzmann, E., Ardhuin, F., & Gallart, J. (2011). Polarized Earth's ambient microseismic noise. *Geochemistry, Geophysics, Geosystems*, *12*, Q07014. https://doi.org/10.1029/2011GC003661

Schulte-Pelkum, V., Earle, P. S., & Vernon, F. L. (2004). Strong directivity of ocean-generated seismic noise. *Geochemistry, Geophysics, Geosystems*, *5*, Q03004. https://doi.org/10.1029/2003GC000520

Sergeant, A., Stutzmann, E., Maggi, A., Schimmel, M., Ardhuin, F., & Obrebski, M. (2013). Frequency-dependent noise sources in the north atlantic ocean. *Geochemistry, Geophysics, Geosystems*, *14*, 5341–5353. https://doi.org/10.1002/2013GC004905

Stehly, L., Campillo, M., & Shapiro, N. (2006). A study of the seismic noise from its long-range correlation properties. *Journal of Geophysical Research*, *111*, B10306. https://doi.org/10.1029/2005JB004237

Stutzmann, E., Ardhuin, F., Schimmel, M., Mangeney, A., & Patau, G. (2012). Modelling long-term seismic noise in various environments. *Geophysical Journal International*, *191*(2), 707–722. https://doi.org/10.1111/j.1365-246x.2012.05638.x

Stutzmann, E., Schimmel, M., Patau, G., & Maggi, A. (2009). Global climate imprint on seismic noise. *Geochemistry, Geophysics, Geosystems*, *10*, Q11004. https://doi.org/10.1029/2009GC002619

Tanimoto, T., Hadziioannou, C., Igel, H., Wasserman, J., Schreiber, U., & Gebauer, A. (2015). Estimate of Rayleigh-to-Love wave ratio in the secondary microseism by colocated ring laser and seismograph. *Geophysical Research Letters*, *42*, 2650–2655. https://doi.org/10.1002/2015GL063637

Toksöz, M. N., & Lacoss, R. T. (1968). Microseisms: Mode structure and sources. *Science*, *159*(3817), 872–873.

Tolman, H. L. (2009). User manual and system documentation of wavewatch iii tm version 3.14. *Technical note, MMAB Contribution*, *276*, 97.

van der Walt, S., Colbert, S. C., & Varoquaux, G. (2011). The numpy array: A structure for efficient numerical computation. *Computing in Science Engineering*, *13*(2), 22–30. https://doi.org/10.1109/MCSE.2011.37

Vinnik, L. (1973). Sources of microseismic *P*-waves. *Pure and Applied Geophysics*, *103*(1), 282–289.

West, M. (2006). The Colima Deep Seismic Experiment, Other/Seismic Network. https://doi.org/10.7914/SN/ZA_2006

Zhang, J., Gerstoft, P., & Bromirski, P. D. (2010). Pelagic and coastal sources of *P*-wave microseisms: Generation under tropical cyclones. *Geophysical Research Letters*, *37*, L15301. https://doi.org/10.1029/2010GL044288

Zhang, J., Gerstoft, P., & Shearer, P. M. (2009). High-frequency *P*-wave seismic noise driven by ocean winds. *Geophysical Research Letters*, *36*, 1–5. https://doi.org/10.1029/2009GL037761

Zhang, J., Gerstoft, P., & Shearer, P. M. (2010). Resolving *P*-wave travel-time anomalies using seismic array observations of oceanic storms. *Earth and Planetary Science Letters*, *292*(3), 419–427.

Supporting Information for "The Effect of Water-Column Resonance on the Spectra of Secondary Microseism P-waves"

Matthias Meschede[1], Eléonore Stutzmann[1], Veronique Farra[1], Martin Schimmel[2], Fabrice Ardhuin[3]

[1]Institut de Physique du Globe de Paris, Paris 75005, France
[2]Institut of Earth Sciences Jaume Almera - CSIC, 08028Barcelona, Spain
[3]University of Brest, CNRS, IRD, Ifremer, Laboratoired'Océanographie Physique et Spatiale, IUEM

1 Table of Matching Strongest Sources

Table S1 lists characteristics of the observed strongest-sources whose geographical origin matches with model R. The table columns correspond to:

(i) the date when the strongest-source was observed.
(ii) the geographical position that corresponds to the strongest-source slowness, assuming that it is a P-wave.
(iii) the cluster label that is assigned to the strongest-source, based on the shape of its beam power spectral density (PSD). The cluster centroids that correspond to a certain type can be seen in Fig. 9a.
(iv) the frequency of the beam-PSD maximum in [Hz].
(v) the beam-PSD maximum in $[m^2/Hz]$.
(vii) the normalized PSD in the frequency range from 0.08-0.3Hz. Faint vertical ticks indicate the position of 0.10Hz, 0.15Hz, 0.20Hz, and 0.25Hz.

Corresponding author: Matthias Meschede, meschede@ipgp.fr

Table S1: observed matching strongest-source properties

date	origin	type	freq.	max.	PSD
06-1-24	59.72N -39.35E	1	0.15	1e-14	
06-1-30	38.76N 178.12E	2	0.20	3e-15	
06-1-31	41.65N -178.27E	3	0.20	2e-15	
06-4-22	-43.47N -36.96E	3	0.19	2e-15	
06-4-23	-43.94N -43.26E	2	0.15	1e-15	
06-5-21	-55.80N -137.31E	1	0.16	2e-15	
06-5-22	-45.78N -137.55E	1	0.16	2e-15	
06-5-29	-40.85N -145.62E	2	0.17	2e-15	
06-6-25	-45.49N -130.11E	1	0.14	3e-15	
06-6-26	-52.25N -131.59E	1	0.15	2e-15	
06-6-27	-39.10N -38.54E	3	0.20	2e-15	
06-7-3	-39.58N -162.86E	0	0.13	2e-15	
06-7-4	-39.58N -162.86E	0	0.13	2e-15	
06-7-8	-4.44N -83.57E	0	0.14	3e-15	
06-7-10	-50.86N -57.36E	1	0.13	2e-15	
06-7-11	-52.33N -50.23E	1	0.14	2e-15	
06-7-18	-43.47N -170.24E	0	0.10	1e-15	
06-7-21	-50.86N -149.84E	1	0.13	1e-15	
06-7-22	-50.86N -149.84E	1	0.14	1e-15	
06-7-24	-43.47N -36.96E	2	0.20	7e-16	
06-7-25	-39.34N -156.99E	4	0.23	1e-15	
06-7-26	-48.62N -143.31E	0	0.13	5e-15	
06-7-27	-52.33N -140.87E	0	0.13	3e-14	
06-7-28	-52.33N -140.87E	0	0.14	1e-14	
06-7-29	-43.94N -43.26E	2	0.19	2e-15	
06-8-19	-34.30N -150.61E	4	0.20	8e-16	
06-8-20	-52.54N -118.11E	0	0.14	1e-15	
06-8-29	-56.70N -51.87E	1	0.14	3e-15	
06-9-3	-41.31N -116.94E	1	0.15	1e-15	
06-9-26	41.65N -178.27E	0	0.12	1e-14	
06-10-6	-43.63N -49.59E	2	0.17	2e-15	
06-10-9	37.24N -161.65E	4	0.20	8e-16	
06-10-12	40.17N -172.65E	4	0.20	7e-16	
06-10-22	-40.85N -145.62E	0	0.12	6e-15	
06-10-31	-41.49N -81.22E	1	0.15	2e-15	
06-11-27	53.50N -3.55E	2	0.18	2e-15	
06-12-21	55.88N -147.20E	1	0.15	9e-15	
08-1-4	62.14N -48.65E	2	0.17	7e-15	
08-1-7	46.22N -178.94E	3	0.20	5e-15	
08-1-8	43.88N 178.81E	3	0.20	4e-15	
08-1-11	45.33N 174.16E	3	0.19	4e-15	
08-1-12	41.45N 177.24E	3	0.19	6e-15	
08-1-14	54.37N 174.06E	2	0.16	2e-15	
08-1-15	60.04N -41.01E	2	0.17	1e-15	
08-1-18	41.45N 177.24E	3	0.20	4e-15	
08-1-19	43.88N 178.81E	3	0.20	4e-15	
08-1-20	41.45N 177.24E	3	0.20	3e-15	
08-1-21	43.88N 178.81E	3	0.20	5e-15	
08-1-23	42.71N 172.30E	3	0.20	3e-15	
08-1-24	45.33N 174.16E	3	0.20	4e-15	
08-1-25	45.33N 174.16E	3	0.20	3e-15	
08-1-26	48.66N 159.30E	2	0.18	5e-15	
08-1-28	66.01N -42.61E	1	0.16	5e-15	
08-1-29	74.75N -38.64E	1	0.15	2e-15	
08-1-31	64.50N -25.57E	0	0.14	6e-15	
08-2-2	62.14N -48.65E	1	0.14	3e-15	
08-2-3	62.14N -48.65E	1	0.16	4e-15	
08-2-4	38.57N 154.17E	2	0.19	3e-15	
08-2-5	44.33N 167.63E	2	0.14	2e-15	
08-2-8	57.38N -34.89E	1	0.14	2e-14	
08-2-9	62.14N -48.65E	0	0.14	7e-15	
08-2-12	41.45N 177.24E	3	0.19	4e-15	
08-2-14	44.33N 167.63E	3	0.20	4e-15	
08-2-17	49.26N 166.00E	3	0.19	2e-15	
08-2-18	49.26N 166.00E	3	0.20	8e-16	
08-2-23	41.41N 166.05E	2	0.19	1e-15	
08-2-24	36.15N -172.69E	3	0.20	3e-15	
08-2-28	51.33N 155.72E	1	0.14	2e-15	
08-2-29	49.26N 166.00E	3	0.20	2e-15	

Continued table

date	origin	type	freq.	max.	PSD
08-3-1	49.75N 172.88E	3	0.20	2e-15	
08-3-3	47.82N 176.71E	3	0.20	3e-15	
08-3-5	64.81N -50.26E	1	0.16	2e-15	
08-3-6	62.14N -48.65E	1	0.15	4e-15	
08-3-7	63.03N -41.04E	1	0.16	1e-15	
08-3-8	63.03N -41.04E	1	0.16	1e-15	
08-3-9	60.04N -41.01E	1	0.16	7e-16	
08-3-13	46.22N -178.94E	3	0.20	2e-15	
08-3-17	42.80N -61.36E	2	0.16	1e-15	
08-3-18	43.88N -56.29E	2	0.17	1e-15	
08-3-21	64.50N -25.57E	1	0.16	8e-16	
08-3-27	63.81N -33.34E	2	0.17	6e-16	
08-3-28	63.03N -41.04E	1	0.16	1e-15	
08-3-29	63.03N -41.04E	1	0.16	1e-15	
08-3-30	60.94N -26.05E	1	0.16	1e-15	
08-4-5	26.52N 165.74E	3	0.20	5e-16	
08-4-6	-38.08N -160.71E	4	0.20	4e-16	
08-4-8	35.62N 142.88E	2	0.19	6e-16	
08-4-9	33.33N 148.21E	3	0.19	2e-15	
08-4-10	35.05N 153.68E	3	0.20	5e-16	
08-4-12	45.42N 156.90E	3	0.20	8e-16	
08-4-13	51.69N 162.54E	3	0.20	3e-15	
08-4-16	41.45N 177.24E	3	0.20	8e-16	
08-4-20	48.40N -175.97E	3	0.20	8e-16	
08-4-21	48.40N -175.97E	3	0.20	4e-16	
08-4-26	5.63N -31.68E	0	0.12	3e-15	
08-4-27	5.63N -31.68E	0	0.13	2e-15	
08-4-28	5.63N -31.68E	1	0.14	4e-16	
08-5-12	30.08N 137.70E	2	0.16	1e-15	
08-5-13	31.65N 142.89E	3	0.19	1e-15	
08-5-17	-40.25N -110.48E	1	0.15	1e-15	
08-5-27	-38.77N -144.39E	4	0.21	4e-16	
08-5-28	-41.35N -139.75E	4	0.21	5e-16	
08-5-29	-40.90N -121.53E	1	0.15	7e-16	
08-5-31	-38.77N -144.39E	4	0.23	4e-16	
08-6-1	-40.90N -121.53E	1	0.12	2e-16	
08-6-2	31.65N 142.89E	3	0.19	1e-16	
08-6-3	35.62N 142.88E	3	0.19	4e-16	
08-6-4	33.33N 148.21E	3	0.19	6e-16	
08-6-7	-28.80N -83.58E	3	0.18	7e-16	
08-6-9	-33.81N -163.05E	4	0.20	7e-16	
08-6-10	-33.81N -163.05E	4	0.20	8e-16	
08-6-26	-39.05N -152.46E	4	0.20	3e-16	
08-6-30	-36.03N -121.14E	1	0.16	8e-16	
08-7-4	-38.77N -93.10E	2	0.16	3e-16	
08-7-6	28.86N -157.99E	3	0.20	2e-16	
08-7-11	-44.84N -109.08E	0	0.13	4e-15	
08-7-12	-45.58N -115.47E	1	0.14	1e-15	
08-7-13	-39.05N -152.46E	0	0.13	7e-16	
08-7-15	-38.77N -144.39E	4	0.20	8e-16	
08-7-23	-29.56N -164.75E	4	0.20	3e-16	
08-7-24	-27.53N -160.08E	4	0.21	3e-16	
08-7-25	-33.81N -163.05E	4	0.20	3e-16	
08-7-26	-31.57N -158.26E	4	0.21	6e-16	
08-7-29	-32.42N -151.44E	4	0.20	7e-16	
08-7-30	-35.77N -148.28E	4	0.20	5e-16	
08-8-2	-35.45N -111.63E	2	0.20	1e-16	
08-8-3	-36.03N -116.34E	2	0.19	1e-16	
08-8-4	-36.03N -116.34E	2	0.18	1e-16	
08-8-16	-35.45N -125.86E	1	0.15	4e-16	
08-8-20	-42.53N -148.38E	4	0.20	6e-16	
08-8-21	-43.41N -134.39E	2	0.14	7e-16	
08-8-23	-40.90N -115.95E	1	0.15	6e-16	
08-8-24	-40.90N -115.95E	1	0.16	2e-16	
08-9-24	63.03N -41.04E	2	0.16	6e-16	
08-9-25	46.32N 163.29E	3	0.19	7e-16	
08-10-8	59.44N -48.52E	0	0.13	4e-15	
08-10-9	60.04N -41.01E	1	0.15	1e-14	
08-10-10	63.03N -41.04E	1	0.16	2e-15	
08-10-20	61.27N -18.57E	1	0.16	2e-15	
08-10-21	43.23N 161.34E	3	0.19	1e-15	
08-10-22	47.13N 169.88E	3	0.19	2e-15	

Continued table

date	origin	type	freq.	max.	PSD
08-10-24	63.03N -41.04E	1	0.15	1e-15	
08-10-27	74.06N -13.14E	1	0.14	2e-15	
08-11-6	47.82N 176.71E	3	0.20	2e-15	
08-11-7	47.82N 176.71E	3	0.20	1e-15	
08-11-8	45.42N 156.90E	3	0.20	6e-16	
08-11-9	44.33N 167.63E	3	0.19	5e-15	
08-11-10	45.33N 174.16E	3	0.20	4e-15	
08-11-11	43.88N 178.81E	3	0.20	1e-15	
08-11-19	42.80N -176.13E	3	0.20	6e-16	
08-11-20	42.80N -176.13E	3	0.20	2e-15	
08-11-21	51.97N 169.56E	2	0.16	2e-15	
08-11-23	54.37N 174.06E	2	0.17	1e-15	
08-11-24	54.16N -178.29E	2	0.17	2e-15	
08-11-25	37.09N 148.46E	3	0.19	2e-15	
08-11-26	42.71N 172.30E	3	0.20	3e-15	
08-11-27	46.22N -178.94E	3	0.20	3e-15	
08-11-28	48.84N -167.53E	0	0.13	3e-15	
08-12-1	47.82N 176.71E	0	0.13	4e-15	
08-12-2	48.40N -175.97E	2	0.14	2e-15	
08-12-3	42.12N -170.49E	3	0.20	1e-15	
08-12-4	64.81N -50.26E	1	0.16	2e-15	
08-12-5	29.41N 164.97E	3	0.19	3e-15	
08-12-6	31.55N 175.95E	4	0.20	1e-15	
08-12-7	38.12N -172.45E	3	0.20	3e-15	
08-12-8	42.12N -170.49E	3	0.20	1e-15	
08-12-10	62.14N -48.65E	1	0.15	2e-15	
08-12-12	33.62N -165.32E	3	0.20	3e-15	
08-12-15	46.32N 163.29E	3	0.19	4e-15	
08-12-18	63.03N -41.04E	0	0.12	8e-16	
08-12-22	57.38N -34.89E	1	0.16	3e-15	
08-12-23	59.44N -48.52E	0	0.13	7e-15	
08-12-27	45.42N 156.90E	2	0.20	2e-15	
08-12-28	43.23N 161.34E	2	0.19	2e-15	
08-12-30	47.13N 169.88E	3	0.19	3e-15	
08-12-31	47.13N 169.88E	3	0.19	3e-15	
11-1-1	40.71N 171.48E	3	0.20	9e-15	
11-1-2	43.55N 173.27E	3	0.20	1e-14	
11-1-3	43.55N 173.27E	3	0.20	7e-15	
11-1-4	40.71N 171.48E	3	0.20	4e-15	
11-1-6	42.72N 166.96E	3	0.19	6e-15	
11-1-8	39.21N -172.39E	3	0.20	7e-15	
11-1-9	40.29N -177.50E	3	0.20	5e-15	
11-1-10	42.65N -175.79E	3	0.20	8e-15	
11-1-16	42.65N -175.79E	3	0.20	9e-15	
11-1-17	44.29N 179.77E	3	0.19	9e-15	
11-1-27	41.74N 177.73E	3	0.19	7e-15	
11-1-28	44.91N -173.41E	3	0.20	5e-15	
11-1-29	45.39N -166.01E	4	0.21	4e-15	
11-1-30	42.65N -175.79E	4	0.20	4e-15	
11-1-31	41.38N -170.92E	3	0.20	1e-14	
11-2-1	43.46N -168.84E	3	0.20	1e-14	
11-2-2	60.22N -34.71E	1	0.14	7e-15	
11-2-6	36.99N -173.34E	3	0.20	8e-15	
11-2-7	36.57N -167.61E	3	0.20	8e-15	
11-2-8	38.54N -166.83E	3	0.20	6e-15	
11-2-11	61.17N -49.78E	0	0.14	2e-14	
11-2-12	59.40N -41.99E	0	0.14	5e-14	
11-2-13	60.95N -27.39E	0	0.12	3e-14	
11-2-15	59.40N -41.99E	0	0.12	1e-14	
11-2-23	59.40N -41.99E	1	0.16	6e-15	
11-2-24	59.40N -41.99E	0	0.14	3e-14	
11-2-25	61.17N -49.78E	0	0.14	8e-15	
11-2-26	41.74N 177.73E	3	0.20	6e-15	
11-3-4	42.72N 166.96E	3	0.19	2e-15	
11-3-5	46.25N 175.72E	3	0.20	1e-15	
11-3-6	46.67N -177.53E	4	0.20	1e-15	
11-3-7	46.96N -170.35E	4	0.20	3e-15	
11-3-8	46.25N 175.72E	3	0.20	2e-15	
11-3-28	40.71N 171.48E	3	0.20	6e-15	
11-3-29	41.74N 177.73E	3	0.20	6e-15	
11-4-15	40.71N 171.48E	3	0.19	2e-15	
11-4-18	41.74N 177.73E	4	0.20	1e-15	

Continued table

date	origin	type	freq.	max.	PSD
11-4-19	40.29N -177.50E	4	0.20	1e-15	
11-4-24	57.85N -21.25E	2	0.17	1e-15	
11-4-25	57.85N -21.25E	2	0.16	6e-16	
11-4-26	-39.97N -158.84E	4	0.22	7e-16	
11-5-3	38.39N 159.49E	3	0.20	1e-15	
11-5-12	40.71N 171.48E	4	0.20	1e-15	
11-5-13	39.08N 176.28E	3	0.20	1e-15	
11-5-14	36.35N 175.37E	4	0.20	9e-16	
11-6-30	-48.14N -118.90E	2	0.16	1e-15	
11-7-4	-44.74N -146.33E	2	0.15	1e-15	
11-7-6	-28.12N -168.39E	4	0.20	1e-15	
11-7-12	11.49N -98.10E	0	0.12	2e-15	
11-7-14	-37.99N -122.82E	2	0.16	2e-15	
11-7-15	-43.46N -118.37E	1	0.16	3e-15	
11-8-1	-44.74N -146.33E	4	0.20	2e-15	
11-8-5	-39.97N -158.84E	4	0.21	2e-15	
11-8-8	-48.14N -112.03E	1	0.15	3e-15	
11-8-9	-47.36N -105.34E	1	0.14	4e-15	
11-8-14	-44.74N -146.33E	4	0.20	2e-15	
11-8-15	-39.97N -158.84E	4	0.21	1e-15	
11-8-16	-44.74N -146.33E	2	0.20	1e-15	
11-9-12	50.92N -26.38E	1	0.15	3e-15	
11-9-13	57.85N -21.25E	2	0.17	2e-15	
11-10-4	69.67N -42.27E	1	0.15	2e-15	
11-10-6	64.52N -27.68E	1	0.16	2e-15	
11-10-15	10.84N -107.20E	0	0.13	2e-15	
11-10-23	34.93N -161.50E	3	0.20	9e-16	
11-10-30	56.48N -42.67E	1	0.14	4e-15	
11-11-17	58.21N -155.89E	1	0.16	4e-15	
11-11-28	66.70N -37.47E	1	0.15	5e-15	
11-11-30	68.06N -29.90E	1	0.14	2e-15	
11-12-1	63.26N 2.93E	2	0.16	3e-15	
11-12-2	36.99N -173.34E	3	0.20	5e-15	
11-12-3	36.99N -173.34E	3	0.20	5e-15	
11-12-4	40.29N -177.50E	3	0.20	9e-15	
11-12-5	41.74N 177.73E	3	0.20	7e-15	
11-12-6	40.71N 171.48E	3	0.20	4e-15	
11-12-8	58.47N -6.86E	2	0.16	2e-15	
11-12-10	58.21N -75.04E	0	0.12	4e-14	
11-12-14	42.65N -175.79E	3	0.20	8e-15	
11-12-15	44.91N -173.41E	3	0.20	7e-15	
11-12-23	44.91N -173.41E	4	0.20	6e-15	
11-12-27	41.74N 177.73E	3	0.20	1e-14	
11-12-28	39.08N 176.28E	3	0.20	6e-15	
11-12-29	36.35N 175.37E	3	0.20	4e-15	
15-1-1	61.62N -32.87E	2	0.16	2e-15	
15-1-5	65.30N -36.08E	1	0.14	4e-15	
15-1-5	61.62N -32.87E	1	0.15	4e-15	
15-1-6	41.48N -163.82E	0	0.13	1e-14	
15-1-7	61.28N -31.97E	1	0.15	6e-15	
15-1-7	61.62N -32.87E	1	0.14	8e-15	
15-1-8	61.62N -32.87E	1	0.15	4e-15	
15-1-8	61.28N -31.97E	2	0.14	3e-15	
15-1-9	59.88N -18.45E	0	0.14	2e-15	
15-1-10	59.88N -18.45E	0	0.14	3e-15	
15-1-10	58.25N -19.47E	0	0.12	1e-15	
15-1-11	56.29N -12.94E	0	0.14	3e-15	
15-1-11	56.83N -13.73E	0	0.12	1e-15	
15-1-12	56.83N -13.73E	0	0.12	2e-15	
15-1-12	59.88N -18.45E	1	0.14	2e-15	
15-1-13	61.62N -32.87E	1	0.14	6e-15	
15-1-14	55.44N -23.51E	2	0.16	4e-15	
15-1-14	58.87N -25.63E	1	0.15	3e-15	
15-1-15	58.87N -25.63E	1	0.14	5e-15	
15-1-15	56.83N -13.73E	2	0.16	6e-15	
15-1-16	58.87N -25.63E	1	0.14	6e-15	
15-1-16	58.25N -19.47E	2	0.16	7e-15	
15-1-18	57.81N -32.62E	1	0.16	3e-15	
15-1-18	56.88N -39.65E	2	0.16	2e-15	
15-1-19	58.87N -25.63E	1	0.14	5e-15	
15-1-19	61.28N -31.97E	1	0.14	4e-15	
15-1-20	58.87N -25.63E	1	0.14	3e-15	

Continued table

date	origin	type	freq.	max.	PSD
15-1-21	57.00N -5.82E	0	0.14	3e-15	
15-1-23	39.35N 153.57E	3	0.19	3e-15	
15-1-26	61.62N -32.87E	0	0.13	6e-15	
15-1-28	72.04N -0.76E	1	0.14	2e-15	
15-1-28	67.85N 6.47E	1	0.14	4e-15	
15-1-29	72.61N -8.24E	0	0.12	8e-15	
15-1-29	65.55N -10.42E	0	0.12	5e-15	
15-1-30	65.55N -10.42E	0	0.12	2e-15	
15-1-30	37.64N 167.93E	3	0.19	3e-15	
15-2-6	42.07N 164.57E	2	0.20	1e-15	
15-2-15	54.92N -33.56E	2	0.14	3e-15	
15-2-17	57.00N -5.82E	1	0.14	1e-15	
15-2-18	57.81N -32.62E	1	0.14	9e-15	
15-2-18	58.91N -35.61E	1	0.14	9e-15	
15-2-19	58.87N -25.63E	0	0.14	2e-14	
15-2-19	61.28N -31.97E	0	0.14	2e-14	
15-2-22	63.97N -28.79E	2	0.20	6e-15	
15-2-22	58.87N -25.63E	1	0.16	4e-15	
15-2-23	58.25N -19.47E	0	0.13	3e-14	
15-2-23	58.87N -25.63E	0	0.14	3e-14	
15-2-24	58.87N -25.63E	1	0.15	4e-15	
15-2-24	61.38N -15.78E	1	0.15	3e-15	
15-2-25	58.87N -25.63E	1	0.16	2e-15	
15-2-25	59.74N -25.52E	2	0.16	1e-15	
15-2-26	58.87N -25.63E	1	0.14	8e-15	
15-2-26	61.28N -31.97E	1	0.14	1e-14	
15-2-27	57.81N -32.62E	0	0.13	1e-14	
15-2-27	58.91N -35.61E	0	0.13	1e-14	
15-2-28	58.87N -25.63E	1	0.14	3e-15	
15-2-28	59.74N -25.52E	1	0.16	1e-15	
15-3-1	58.87N -25.63E	2	0.17	1e-15	
15-3-2	58.87N -25.63E	2	0.16	2e-15	
15-3-3	58.87N -25.63E	2	0.16	9e-16	
15-3-4	51.58N -42.72E	1	0.14	2e-15	
15-3-4	49.92N -42.10E	1	0.15	3e-15	
15-3-5	54.92N -33.56E	1	0.16	1e-15	
15-3-5	56.70N -39.44E	0	0.12	2e-15	
15-3-6	62.84N -38.94E	1	0.16	2e-15	
15-3-6	57.81N -32.62E	1	0.14	2e-15	
15-3-7	61.28N -31.97E	1	0.16	2e-15	
15-3-7	58.87N -25.63E	1	0.14	3e-15	
15-3-8	63.97N -28.79E	1	0.16	2e-15	
15-3-8	61.62N -32.87E	1	0.14	2e-15	
15-3-9	58.87N -25.63E	1	0.14	1e-15	
15-3-10	40.49N 151.72E	3	0.18	1e-15	
15-3-10	35.84N 144.55E	3	0.19	2e-15	
15-3-12	58.87N -25.63E	1	0.16	3e-15	
15-3-12	58.25N -19.47E	1	0.16	3e-15	
15-3-14	58.87N -25.63E	1	0.14	3e-15	
15-3-15	59.88N -18.45E	1	0.14	3e-15	
15-3-16	61.62N -32.87E	1	0.16	2e-15	
15-3-19	61.62N -32.87E	1	0.15	6e-15	
15-3-19	61.28N -31.97E	1	0.15	4e-15	
15-3-20	61.62N -32.87E	1	0.14	5e-15	
15-3-20	61.28N -31.97E	1	0.16	2e-15	
15-3-21	54.92N -33.56E	2	0.15	9e-16	
15-3-21	57.81N -32.62E	1	0.15	2e-15	
15-3-22	-49.34N -114.21E	1	0.16	1e-15	
15-3-22	40.39N -27.13E	2	0.16	3e-16	
15-3-25	-49.70N -83.16E	1	0.16	3e-15	
15-3-31	60.19N -9.83E	2	0.16	9e-16	
15-4-13	57.15N -29.36E	2	0.16	2e-15	
15-4-21	41.55N -37.19E	2	0.15	1e-15	
15-4-22	45.36N -36.92E	4	0.14	5e-16	
15-4-25	29.95N -167.50E	4	0.20	5e-16	
15-4-29	44.30N -42.10E	4	0.21	4e-16	
15-5-11	59.88N -18.45E	2	0.16	1e-15	
15-5-11	56.83N -13.73E	2	0.18	6e-16	
15-5-12	60.19N -9.83E	2	0.18	4e-16	
15-5-16	63.97N -28.79E	2	0.18	3e-16	
15-5-17	59.74N -25.52E	2	0.18	7e-16	
15-5-18	-45.89N -155.72E	1	0.14	2e-15	

Continued table

date	origin	type	freq.	max.	PSD
15-5-31	62.65N -22.07E	4	0.20	1e-16	
15-6-1	62.65N -22.07E	2	0.20	1e-16	
15-6-12	-36.28N -149.04E	2	0.16	6e-16	
15-6-19	-39.40N -153.61E	4	0.21	5e-16	
15-6-20	-35.78N -142.32E	4	0.23	3e-16	
15-6-24	-30.82N -167.93E	4	0.20	1e-15	
15-6-25	-35.23N -167.46E	4	0.20	6e-16	
15-6-26	-41.98N -158.74E	4	0.21	5e-16	
15-6-29	-42.99N -84.30E	0	0.13	4e-16	
15-6-30	-32.73N -83.66E	0	0.13	3e-16	
15-7-2	14.25N 156.80E	4	0.21	3e-16	
15-7-3	8.80N 154.19E	4	0.20	4e-16	
15-7-3	14.01N 150.09E	4	0.19	3e-16	
15-7-4	12.61N 152.43E	3	0.20	5e-16	
15-7-4	19.10N 148.83E	4	0.20	3e-16	
15-7-8	14.82N 146.42E	2	0.16	8e-16	
15-7-10	27.35N 132.31E	3	0.20	5e-16	
15-7-12	23.51N 137.24E	4	0.20	2e-16	
15-7-15	27.85N 140.39E	4	0.20	2e-16	
15-7-22	-21.16N -80.51E	0	0.12	7e-16	
15-7-25	-42.58N -104.40E	0	0.14	2e-15	
15-7-26	-24.84N -103.58E	0	0.14	1e-15	
15-7-27	-15.75N -92.04E	1	0.16	1e-15	
15-8-5	21.98N 139.96E	4	0.22	2e-16	
15-8-6	21.04N 131.50E	3	0.20	6e-16	
15-8-6	-46.28N -88.23E	0	0.13	5e-16	
15-8-7	23.22N 128.91E	3	0.20	5e-16	
15-8-8	25.63N 126.53E	3	0.20	2e-16	
15-8-12	-39.58N -146.15E	4	0.20	7e-16	
15-8-13	61.28N -31.97E	1	0.16	4e-16	
15-8-14	-39.58N -146.15E	4	0.21	6e-16	
15-8-16	19.56N 161.44E	4	0.20	2e-16	
15-8-17	14.70N 156.98E	3	0.20	1e-15	
15-8-17	19.56N 161.44E	3	0.20	3e-16	
15-8-19	12.61N 152.43E	3	0.18	3e-15	
15-8-19	23.42N 154.05E	3	0.20	7e-16	
15-8-20	20.50N 149.99E	3	0.20	1e-15	
15-8-20	24.36N 148.28E	3	0.19	5e-16	
15-8-21	25.25N 145.53E	3	0.19	8e-16	
15-8-21	23.28N 144.31E	3	0.19	1e-15	
15-8-22	26.42N 142.89E	4	0.20	7e-16	
15-8-23	-49.34N -120.69E	1	0.14	3e-15	
15-8-23	25.25N 145.53E	4	0.23	4e-15	
15-8-24	32.50N 149.46E	3	0.19	1e-15	
15-8-24	35.09N 149.57E	4	0.18	9e-16	
15-8-25	38.44N 155.60E	3	0.19	1e-15	
15-8-25	32.50N 149.46E	3	0.19	1e-15	
15-8-26	42.93N 160.26E	3	0.20	8e-16	
15-8-26	32.50N 149.46E	1	0.16	1e-15	
15-8-31	23.29N -178.54E	4	0.20	4e-16	
15-9-1	-39.47N -119.76E	1	0.15	1e-14	
15-9-2	12.98N -143.64E	4	0.20	6e-16	
15-9-3	12.98N -143.64E	4	0.20	9e-16	
15-9-4	12.98N -143.64E	4	0.20	5e-16	
15-9-6	27.57N 172.14E	4	0.19	5e-16	
15-9-7	30.78N 170.97E	3	0.19	6e-16	
15-9-8	32.86N 164.67E	3	0.19	1e-15	
15-9-11	36.41N 150.30E	3	0.19	2e-15	
15-9-14	36.58N -179.32E	4	0.20	5e-16	
15-9-14	37.34N -175.38E	4	0.20	8e-16	
15-9-15	36.58N -179.32E	4	0.21	2e-16	
15-9-19	54.92N -33.56E	4	0.20	9e-17	
15-9-20	58.87N -25.63E	2	0.17	3e-16	
15-9-21	42.36N 162.30E	4	0.20	2e-16	
15-9-21	37.03N 156.15E	3	0.20	2e-16	
15-9-22	42.93N 160.26E	3	0.20	3e-16	
15-9-23	42.93N 160.26E	4	0.20	4e-16	
15-9-23	40.57N 157.81E	3	0.20	6e-16	
15-9-25	43.38N 173.06E	3	0.20	3e-16	
15-9-26	25.30N 134.68E	3	0.20	2e-16	
15-9-27	25.30N 134.68E	4	0.19	1e-16	
15-10-4	20.43N 164.59E	4	0.20	9e-16	

Continued table

date	origin	type	freq.	max.	PSD
15-10-5	23.65N 160.03E	3	0.20	2e-15	
15-10-6	28.03N 156.46E	3	0.20	1e-15	
15-10-7	33.35N 154.19E	3	0.19	2e-15	
15-10-8	38.44N 155.60E	3	0.18	3e-15	
15-10-9	39.35N 153.57E	4	0.19	9e-16	
15-10-9	-44.48N -114.73E	1	0.15	9e-15	
15-10-10	-49.34N -114.21E	0	0.14	1e-14	
15-10-18	21.98N 139.96E	4	0.21	4e-16	
15-10-19	23.51N 137.24E	4	0.22	4e-16	
15-10-20	40.35N -47.98E	4	0.22	6e-16	
15-10-21	56.70N -39.44E	2	0.17	1e-15	
15-10-21	54.92N -33.56E	4	0.20	2e-15	
15-10-22	59.88N -18.45E	1	0.14	2e-15	
15-10-23	59.74N -25.52E	2	0.16	9e-16	
15-10-26	55.44N -23.51E	0	0.15	6e-15	
15-10-29	57.15N -29.36E	3	0.19	2e-15	
15-11-4	55.44N -23.51E	1	0.15	5e-15	
15-11-11	57.70N 1.43E	1	0.14	6e-15	
15-11-22	49.92N 167.20E	1	0.15	2e-15	
15-11-23	52.37N 172.01E	1	0.14	1e-15	
15-12-1	57.15N -29.36E	4	0.12	4e-15	
15-12-1	59.88N -18.45E	0	0.12	8e-15	
15-12-3	62.98N -25.69E	0	0.12	8e-15	
15-12-7	56.83N -13.73E	1	0.14	3e-15	
15-12-7	56.29N -12.94E	0	0.13	2e-14	
15-12-8	58.25N -19.47E	1	0.16	5e-15	
15-12-9	62.98N -25.69E	0	0.13	9e-15	
15-12-12	42.93N 160.26E	3	0.19	3e-15	
15-12-13	42.93N 160.26E	0	0.13	2e-15	
15-12-21	58.87N -25.63E	0	0.14	8e-15	
15-12-23	59.88N -18.45E	1	0.14	5e-15	
15-12-24	67.81N -3.18E	2	0.16	2e-15	
15-12-25	67.12N 3.20E	2	0.15	3e-15	
15-12-26	47.08N 163.26E	1	0.15	5e-15	
15-12-29	55.57N -19.95E	0	0.13	4e-15	
15-12-30	59.88N -18.45E	0	0.13	7e-15	
15-12-30	49.44N -2.20E	1	0.14	2e-14	
15-12-31	58.87N -25.63E	0	0.14	6e-15	